

Persistent infrared spectral hole burning of NO⁻ 2 ions in potassium halide crystals. I. Principle and satellite hole generation

W. P. Ambrose, J. P. Sethna, and A. J. Sievers

Citation: *The Journal of Chemical Physics* **95**, 8816 (1991); doi: 10.1063/1.461216

View online: <http://dx.doi.org/10.1063/1.461216>

View Table of Contents: <http://scitation.aip.org/content/aip/journal/jcp/95/12?ver=pdfcov>

Published by the [AIP Publishing](#)

Articles you may be interested in

[Persistent spectral hole burning in europium-doped sodium tellurite glass](#)

Appl. Phys. Lett. **87**, 091107 (2005); 10.1063/1.2035884

[Persistent infrared hole burning spectroscopy of NH₃D⁺ doped in \[\(NH₄\)_x,Rb_{1-x}\]SO₄ mixed crystals](#)

J. Chem. Phys. **99**, 5661 (1993); 10.1063/1.465961

[Persistent spectral holeburning, luminescence line narrowing and selective excitation spectroscopy of the R lines of Cr\(III\) tris\(2,2'bipyridine\) in amorphous hosts](#)

J. Chem. Phys. **97**, 7902 (1992); 10.1063/1.463465

[Subnanosecond burning of persistent spectral holes by donoracceptor electron transfer in tetraphenylporphine/pbenzoquinone systems](#)

Appl. Phys. Lett. **59**, 1814 (1991); 10.1063/1.106207

[Ultrasonic modulation of persistent spectral holes in crystals](#)

Appl. Phys. Lett. **43**, 437 (1983); 10.1063/1.94380



Persistent infrared spectral hole burning of NO_2^- ions in potassium halide crystals. I. Principle and satellite hole generation

W. P. Ambrose,^{a)} J. P. Sethna, and A. J. Sievers

Laboratory of Atomic and Solid State Physics and Materials Science Center, Cornell University, Ithaca, New York 14853

(Received 30 July 1991; accepted 9 September 1991)

New features are resolved within the internal vibrational mode spectra of NO_2^- defects in KCl, KBr, and KI crystals at low temperatures using high-resolution Fourier transform spectroscopy and persistent infrared spectral hole (PIRSH) burning separately and together. With interferometry it has been discovered that the vibrational linewidths of the different modes range over a factor of 300—from 0.01 cm^{-1} to $\sim 3\text{ cm}^{-1}$ and, with PIRSH burning, it has been demonstrated that the narrowest lines are inhomogeneously broadened while the broadest ones are homogeneously broadened. PIRSH's have been found in some internal modes and combination bands of the NO_2^- molecule when pumped with low-intensity single-mode lead salt diode lasers; however, detectable persistent holes are not produced in all of the modes because of a competition between hole production and relaxation by tunneling at low temperatures. This competition results in a hole burning intensity, below which hole relaxation overwhelms hole production and only small holes may be produced. The most unusually shaped absorption features are the V-shaped notches in the reorientational tunneling fine structure at the NO_2^- bending mode frequency in KCl and KBr. Of all the internal modes that do show pronounced PIRSH burning, these V-notched absorption bands exhibit the most striking behavior. Multiple satellite PIRSH's are detected at frequencies away from the single-mode laser burn frequency with a broadband probe beam produced by a high-resolution Fourier transform interferometer. An explanation for these satellite holes is derived from temperature, plastic deformation, and uniaxial stress dependence measurements on the KCl: NO_2^- absorption spectrum. We find that the inhomogeneous broadening of the KCl: NO_2^- ν_2 reorientational tunneling fine structure is dominated by degenerate rotor level splitting produced by random crystal strains. Degenerate perturbation theory of the rotor level splitting in the strain field is found to match very closely the V-shaped inhomogeneous distribution of levels associated with the KCl: NO_2^- reorientational tunneling fine structure. The general conclusion is that whenever strain splitting of a doubly degenerate level dominates the inhomogeneous broadening, then the absorption spectrum displays zero strength in the distribution at zero splitting and a linear increase in absorption coefficient away from this frequency generating the observed V-shaped notch in the absorption profile.

I. INTRODUCTION

When NO_2^- ions are doped into alkali halide crystals, a complex electronic and vibrational spectrum appears extending from the ultraviolet (UV) to the far infrared (FIR). The low symmetry of the defect ion allows a large number of different spectroscopic probes to be used successfully to excite this defect-lattice system in different ways. In comparative reviews of defects in crystals,¹⁻⁴ it is agreed that concomitant with the large number of possible probe techniques, NO_2^- ions exhibit more complex behavior than atomic or diatomic defects. For each molecule-host combination, the underlying character of the spectra is that the singlet electronic energy levels produce transitions in ultraviolet absorption and emission;⁵⁻²³ the spin triplet electronic levels produce emission lines in the visible;^{18,19,24,25} the three internal vibrational modes produce lines in infrared absorp-

tion²⁶⁻³³ and Raman scattering;^{10,13,14,18,21,34-39} and the librational and local modes (external vibrational modes) produce lines in far-infrared absorption^{3,40-46} and Raman scattering.^{10,18,39,47} However, this characterization of the different transitions only identifies the main sequences in each of the frequency regions. Since the electronic levels, internal vibrational levels, librational, local, and tunneling modes are all coupled to each other, the resultant spectrum contains a great deal of additional fine structure. It has long been recognized that a complete theoretical identification of this complex and intricate experimentally determined fine structure over such a large frequency range would translate into the first complete, detailed description of the dynamics of a simple low-symmetry molecule-lattice system. This challenge still exists today.

Although these efforts have lead to a general qualitative picture of the molecule dynamics in the solid, there are still inconsistencies in the results obtained with different techniques and hence in the proposed model explanations. For example, from infrared (IR) absorption,²⁶ Raman scatter-

^{a)} Present address: Los Alamos National Laboratory, Los Alamos, NM 87545.

ing,^{13,21,34-36} ultraviolet absorption,^{7,8,10,11,13,20,21-23} and ultraviolet emission studies,^{7-9,13,15,21} it is generally agreed that the NO_2^- molecule performs tunneling connected with rotation about a preferred axis in some potassium halides at low temperatures, but hindered rotor model fits to these measured spectra give inconsistent rotor level spacings and selection rules.^{7,10,11,13,21,22,26,48,49}

The discovery⁴⁴⁻⁴⁶ and detailed characterization of persistent IR spectral holes (PIRSH's) in the internal mode spectrum of NO_2^- doped potassium halide crystals, the topic of this paper, provides a new opportunity to investigate the IR internal vibrational modes and associated fine structure from an ultra-high-resolution vantage point. The width of such a spectral hole is twice the homogeneous width if no additional sources of hole broadening are present, such as power broadening or spectral diffusion. The homogeneous width is determined by the excited state dephasing time, which, at low temperatures, becomes excited state lifetime limited. Hence, this IR technique permits, for the first time, the testing of homogeneous versus inhomogeneous broadening for the different vibrational modes and the possibility of exploring narrow features characteristic of the homogeneous width inside inhomogeneously broadened lines.

Before the high-resolution capability of the diode laser probing technique can be used, low-temperature high-resolution infrared NO_2^- absorption spectra must be obtained in order to determine precisely the frequencies of interest. In making such measurements with state-of-the-art interferometers, we have discovered that these high-resolution spectral maps, in themselves, provide new information about the location, size, shape, and spacing of the IR fine structure not previously obtained with grating instruments.

Once the high-resolution features are located with interferometers, then PIRSH burning can be attempted with Pb salt diode lasers. We find that persistent changes can be induced in some of the main internal vibrational transitions, in combination bands and in the fine structure near each vibrational transition. It is found that not all IR modes undergo persistent changes and of those that do, not all are inhomogeneously broadened. A minimum burn intensity for persistent holes has been identified in terms of simple model parameters to account for the variability of the PIRSH effect. Finally, our observation and study of persistent multiple infrared satellite holes in the ν_2 internal bending mode spectrum of NO_2^- in KCl has been used to show that the different transition frequencies within the inhomogeneously broadened fine structure are completely correlated with each other. Our model shows that they definitely stem from single axis rotational motion of isolated molecules at low temperature.

Section II focuses on the new experimental techniques. After describing the optical setup and the detection techniques for holes and antihole, we show how the hole burning can be used in conjunction with high-resolution Fourier transform spectroscopy to extend a new kind of pump-probe experiment.

Section III presents a variety of IR spectra for the NO_2^- lattice system. In Sec. III A, high-resolution low-temperature IR absorption spectra for the nitrite ion in KI, KBr, and

KCl are presented. The frequency regions cover the ν_1 symmetric stretch mode, the ν_2 symmetric bending mode, the ν_3 antisymmetric stretch mode, and the $[\nu_2 + \nu_3]$ and the $[\nu_1 + \nu_3]$ vibrational combination modes. Of particular interest for the later part of this paper are a pair of V-shaped notches resolved for the first time in the inhomogeneously broadened tunneling sidebands of the ν_2 mode in KCl and KBr. Spectral hole burning attempts were made on all of these modes and the detailed experimental findings are presented in Sec. III B. PIRSH burning is found to occur in the ν_1 , ν_2 , ν_3 , and $[\nu_2 + \nu_3]$ modes of $\text{KI}:\text{NO}_2^-$. However, for $\text{KBr}:\text{NO}_2^-$ and $\text{KCl}:\text{NO}_2^-$ PIRSH burning occurs in the ν_2 and ν_3 modes, but not in the ν_1 and $[\nu_2 + \nu_3]$ modes at the maximum diode laser intensity available to us, namely, 25 mW/cm^2 . These experiments illustrate that the dynamics behind the V-shaped notches in the absorption spectrum of the ν_2 mode are very different from the rest of the PIRSH burning results. It is found that a hole burned in the notched reorientational tunneling sidebands of ν_2 in $\text{KCl}:\text{NO}_2^-$ produces satellite holes away from the laser burn frequency. This result is unlike that found in any other infrared hole burning system measured to date. Temperature, plastic deformation, and uniaxial stress dependence of the $\text{KCl}:\text{NO}_2^-$ ν_2 infrared absorption spectrum are used to experimentally construct, without model assumptions, the reorientational tunneling-vibrational level diagram associated with this system. The resultant diagram complements the lower resolution version constructed by Avarmaa and Rebane from temperature-dependent UV absorption spectra.^{7,13}

Section IV presents analyses and discussion of experimental results. A calculation for the hole depth that results from a competition between hole formation and relaxation processes is found to describe the $\text{KI}:\text{NO}_2^-$ PIRSH depth intensity dependence (Secs. IV A-IV C). A comparison of NO_2^- hole burning results in the different hosts is made in Sec. IV D based on the measured hole depth intensity dependence. The experimentally derived reorientational tunneling-vibrational-level diagram for $\text{KCl}:\text{NO}_2^-$ is used to explain the origin of the infrared sideband satellite holes in Sec. IV E. The V-notched inhomogeneous tunneling sideband line shapes are then calculated using the nonlinear splitting behavior of degenerate rotor levels under the influence of normally distributed lattice strains (Sec. IV F).

The conclusions, which contain a summary of the main points and suggestions for additional work, are given in Sec. V.

II. EXPERIMENTAL DETAILS

A. Samples

All of the spectroscopic experiments were performed on single-crystal alkali halide samples doped with NO_2^- and/or NO_3^- . Boules of KCl, KBr, or KI were grown in an argon atmosphere by the Czochralski method and were doped by adding potassium nitrite or nitrate dopant to the melt. The list of boules used in this work is given in Table I. Nominal dopant concentrations were in the range of 0.02 mole % to 0.1 mole %. Isotopically substituted molecules were also doped into KI crystals to replace the > 99% naturally abun-

TABLE I. Single-crystal boule list.

Nominal concentration	Boule number
KI + 0.05% KNO_2	8601156W
KI + 0.02% KNO_3 (40% ^{18}O)	8805105W
KI + 0.1% KNO_3 (40% ^{18}O)	8804215W
KBr + 0.05% KNO_2	8601176W
KCl + 0.05% KNO_2	8601086W

dant species $^{14}\text{N}^{16}\text{O}_2^-$ and $^{14}\text{N}^{16}\text{O}_3^-$. Only 40% enriched $\text{K}^{14}\text{N}^{18}\text{O}_3$ was available as a dopant. KI crystals doped with $\text{K}^{14}\text{N}^{18}\text{O}_3$ contained NO_2^- and NO_3^- molecular ions with all combinations of ^{16}O and ^{18}O with ^{14}N .⁵⁰

The impurity dopant concentrations are determined from the known strength of the infrared stretch-band absorption band at room temperature,²⁶ or from the $[\nu_2 + \nu_3]$ vibrational combination band with the sample at 1.5 K. For the $[\nu_2 + \nu_3]$ mode, the relation between the molecule concentration, N , and the peak absorption coefficient, α_p , or the integrated peak area $S = \int \alpha(\nu) d\nu$, is

$$N = [(3.6 \pm 0.2) \times 10^{17} \text{ ions/cm}^2] \alpha_p$$

$$= [(8 \pm 1) \times 10^{18} \text{ ions/cm}] S,$$

which is based on the room-temperature stretch-mode calibration.²⁶ Boules intentionally doped with either KNO_2 or KNO_3 and grown under an atmosphere of argon had about 100 times more NO_2^- than NO_3^- (KNO_3 decomposes to KNO_2 near 400 °C). The concentration of both species tended to increase toward the bottom of a boule, and the relative concentration of NO_3^- to NO_2^- also increased. For various studies, samples were cleaved along $\{100\}$ faces, machined into 0.5 inch or 2.5 mm diameter rods, cut and polished along $\{110\}$ faces, or cleaved and then plastically deformed by pressing them at 100 °C along a $[100]$ direction.

B. Persistent IR hole burning with tunable diode lasers

1. Laser source optics

Figure 1 shows the experimental set up used to search for and study PIRSH burning at low temperatures. Manipulation of the tunable lead salt diode laser (DL) beam occupies the upper third of the figure. The diodes are mounted on the cold finger of a closed-cycle refrigerator or cold head, wherein they are coarsely temperature tuned with a cryogenic temperature stabilizer (CTS) from 14 to about 100 K with a temperature tuning rate on the order of $+1 \text{ cm}^{-1}/\text{deg}$. Temperature tuning is a slow processes. More rapid current tuning is accomplished with the laser control module (LCM). Infrared lead salt diode lasers are current tuned at typically 30 to 300 MHz/mA and tune over a large fraction of a cm^{-1} (several GHz) without a mode hop for modulation frequencies up to at least 1 MHz.

The diodes lasers are cleaved cavities approximately 100 to 200 μm on a side, with a laser spot size at the diode of about 25 to 100 μm . This parallel mirror cavity produces multimode lasing well above threshold with several strong modes spaced on the order of 1 to 10 cm^{-1} in the cleaner,

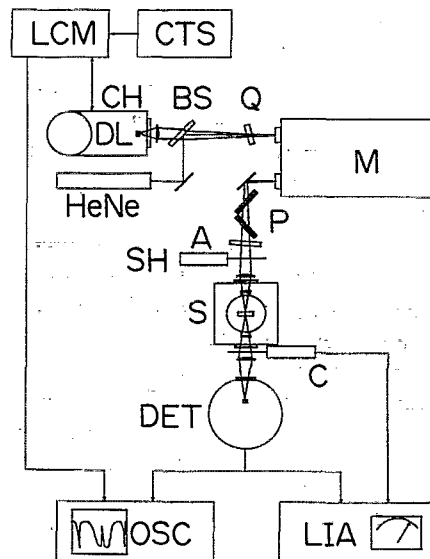


FIG. 1. Experimental apparatus for studying persistent infrared spectral hole burning at low temperatures. The labels are defined as follows. DL, tunable infrared semiconductor diode laser; LCM, laser control module for fine current tuning of the diode laser; CTS, cryogenic temperature stabilizer for coarse temperature tuning of the diode laser; CH, cold head which contains the diode laser; HeNe, helium-neon alignment laser; BS, NaCl beam splitter for combining the red and infrared beams; Q, quarter wave plate; M, monochromator for coarse calibration of the diode frequency and diode laser mode filtering; P, pile of plates polarizer; A, Attenuators; SH, shutter for blocking the beams; S, sample held in a Janis supervaritemp cryostat; C, chopper; DET, InSb, HgCdTe, or Ge:Cu detector; OSC, digital storage scope for storing hole burned spectra; LIA, lock-in amplifier for monitoring the sample transmittance at a fixed frequency.

lower power diode lasers (total power $< 100 \mu\text{W}$). The small cavity geometry also produces a strongly diverging beam at the output, which when collimated with a fast lens produces a doughnut-shaped intensity profile.

To arrange the IR optics, a helium-neon laser (HeNe) is first aligned collinearly with the focused diode beam using a HgCdTe detector, then optical components transparent to visible and IR are placed in the visible laser beam. Since different diode laser modes have a strong angular variation in the vertical direction, it is preferable to align the optics while operating the diode near the frequency of the experiment.

A Jarrell-Ash 3/4 meter monochromator (M) with a 50 line/mm grating is used to coarsely frequency calibrate a diode and filter out the unwanted multimode behavior. The practical resolution of the monochromator is greater than a tenth of a wave number or a few GHz. Finer relative frequency calibration of the diode laser is accomplished with a 1 in germanium etalon (free spectral range $= 1/2nd = 0.05 \text{ cm}^{-1} = 1.5 \text{ GHz}$).

An insidious problem for high-power diodes is a multimode feature that occurs with a closer mode spacing of a few hundred MHz than for low-power diodes (in addition to the 1 to 10 cm^{-1} spacing in lower-power diodes). Very often the power in each mode is no more than that found in a low-power diode laser—there are just more modes. The mono-

chromator simultaneously passes several of these closely spaced modes, and they can be easily mistaken for a single mode. This feature gives false spectra, and produces several closely spaced holes in a hole burning experiment. Fortunately, the presence of this behavior can be detected by observing the fringe behavior in the etalon spectrum. As the angle between the etalon and the laser beam axis is varied, a train of fringes with roughly constant fringe spacing and intensity will march across the oscilloscope. If several modes spaced less than a GHz are lasing, then the fringes will exhibit an oscillatory amplitude.

Lead salt diode lasers do not like to look at their own reflections—especially the higher-power varieties. A few percent of the output power fed back into a diode laser produces high-frequency amplitude noise or “fuzz.”⁵¹ A fuzzy diode does not burn holes and has no etalon fringes, i.e., it appears to be frequency broadened. To avoid a fuzzy output from a diode, optical components are tilted slightly so that the reflected beam does not return to the diode laser. The biggest feedback offenders are the slits on the mono chromator. A quarter wave plate (Q) provides optical isolation from slit reflections. Circularly polarized reflected light returning to the diode laser emerges from the quarter wave plate as linearly polarized light, but at 90° to the original polarization. This polarization rotated feedback does not couple to the diode gain medium producing this mode. Hence, the quarter wave plate is used to eliminate feedback instabilities, as well as to change the polarization of the IR beam for polarization dependent studies in combination with the Brewster's angle pile-of-plates polarizer (P).

For PIRSH measurements it is useful to probe a spectral feature at low intensity, or to let it sit in the dark. Hence, CaF_2 or thin-metal-film attenuators (A) and a shutter (SH) are employed to vary the intensity of the beam. Electronic timing of the shutter period is used to reproducibly illuminate the sample. The diode laser beam, which has been filtered, polarization modified, and attenuated with thin metal-film attenuators, is focused into a sample which is held in a superfluid He bath in an optical immersion cryostat, and the transmitted IR light is then detected.

2. Detection of holes and antiholes with diode lasers

The detectors used in our study are InSb, HgCdTe, and Ge:Cu photodetectors. Their detectivities peak near 5, 10, and $20\ \mu\text{m}$, respectively, with a sharp drop in detectivity just below the peak (characteristic of a semiconductor band gap). The first two are optimized to work near liquid-nitrogen (77 K) temperature and the Ge:Cu detector works best just above liquid-helium (4.2 K) temperature. The preamplifier feedback resistors are selected to provide about a 1 MHz electrical bandwidth. To reduce the thermal noise of the preamplifier stage, the FET amplifier and feedback resistor are mounted in the detector cryostat along with the detector for the InSb and the Ge:Cu detectors. These two detectors are blackbody background shot noise limited, and benefit from cold apertures ($f/3$ in each case) and cold filtering to reduce the blackbody photon noise.

The detection system in Fig. 1 includes a chopper (C) and lock-in amplifier or a Tektronix 7D20 digital oscillo-

scope (OSC), which is connected to an HP computer via an HPIB interface. To search for PIRSH's, the storage scope is used first to perform spectroscopy in real time by modulating the diode laser current and displaying and averaging the detected power spectrum. Sample absorptions are identified by moving the sample in and out of the laser beam. Then, a hole growth curve is obtained by tuning the diode laser into a spectral feature and fixing the current. The temporal behavior of the transmitted power is obtained by chopping the transmitted beam, and lock-in detecting with an effective narrow passband about the chopper frequency. The lock-in signal amplitude is displayed on a chart recorder. If a persistent spectral change is detected, the chopper is stopped and the diode laser current is once again modulated to record a new power spectrum. Comparing the two power spectra reveals the shape of the PIRSH.

C. Simultaneous hole burning and interferometry

Figure 2 shows, from a top view, how the diode laser optics are combined with a Bomem interferometer and a liquid-helium cooled sample to perform combined diode laser hole burning and high-resolution IR Fourier transform spectroscopy (FTS) experiments. For experiments where the IR vibrational mode to be hole burned is well separated in frequency from other vibrational modes, the monochromator is not necessary to filter out the multiple modes of the diode laser, since spectroscopy is not being performed with the diode laser. In experiments where there is a possibility of

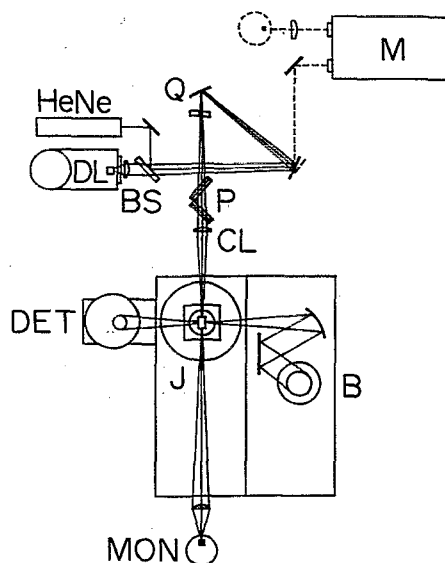


FIG. 2. Experimental setup for simultaneous hole burning and high-resolution spectroscopy with an IR interferometer. The optics at the level of the sample chamber are shown. Diode laser DL and helium-neon HeNe beams are combined with a NaCl beam splitter. A quarter wave plate Q and polarizer P are used to orient the diode laser polarization at any angle. Tuning the diode laser is performed while temporarily diverting the diode laser beam into the monochromator M . A Janis supervaritemp cryostat J is inserted into the Bomem interferometer B . The sample is positioned in the Bomem beam, which passes from right to left in the figure, and then the diode laser beam is focused near the sample. The interferometer detector DET is a Ge:Cu photodetector. Hole burning progress is monitored with a HgCdTe detector MON.

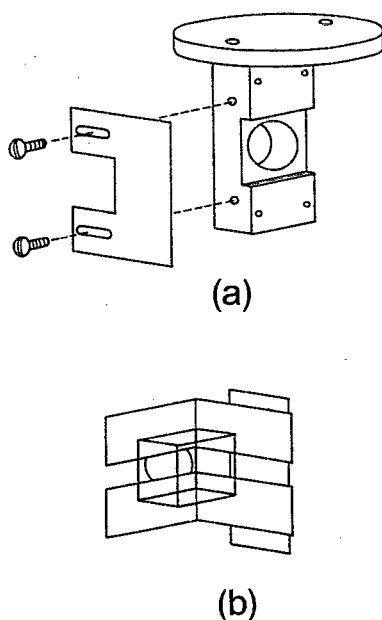


FIG. 3. Sample holder designs for simultaneous spectroscopy and hole burning. In both (a) and (b), the diode laser and interferometer beams probe the sample at a right angle. Foil masks insure that diode laser light only passes through the portion of the sample probed by the interferometer. (a) A single sample is wired over the hole in the slot, and a mask is fastened with screws. (b) Rather than make a new holder for each experiment, a sample *cleaved* to any size is masked with foil.

burning more than one defect mode, for example, in the tunneling fine structure of $\text{KCl}:\text{NO}_2^-$, the monochromator is included in the diode laser-beam path before the sample.

Sample holder design plays an important role in the combined PIRSH plus FTS experiments. The chief criterion is that the volume of sample that is pumped by the diode laser is limited to the volume probed by the interferometer. The larger the volume pumped at a given power, the weaker the hole that is produced. (See the persistent hole burning results for $\text{KI}:\text{NO}_2^-$.) Figure 3 shows the sample holder designs which trade off potential hole depth for ease in sample preparation and cryostat alignment. The sample masks are made sufficiently large so that light arriving at either detector must come through the sample.

III. EXPERIMENTAL RESULTS

A. High-resolution infrared spectra of NO_2^- in KCl, KBr, and KI

The three internal normal modes of the NO_2^- ion are shown schematically in Fig. 4(a). (The nitrogen atom is in the middle, the bond lengths are 1.24 \AA , and the molecule is bent with an angle of about 116° to 120° in the electronic ground state.²⁶) The vibrational modes consist of the symmetric and antisymmetric stretch modes ν_1 and ν_3 and the symmetric bending mode ν_2 . In the electronic ground state, the stretch modes lie in the 1300 cm^{-1} region and the bending mode is near 800 cm^{-1} .

The vibrational-mode transition-dipole-moment direc-

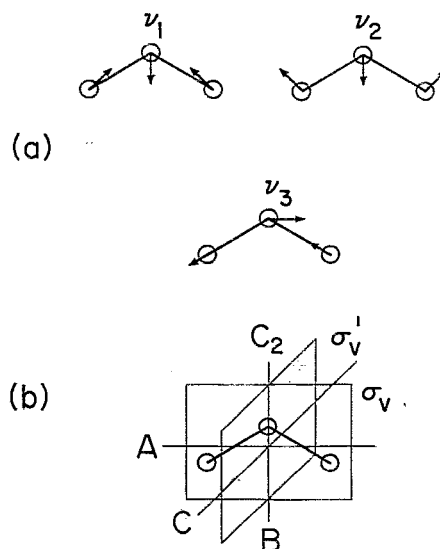


FIG. 4. NO_2^- internal vibrational modes and molecule symmetry elements. (a) The three normal modes: ν_2 (A_1) bending mode ($\sim 800 \text{ cm}^{-1}$), ν_1 (A_1) symmetric stretch mode ($\sim 1325 \text{ cm}^{-1}$), and ν_3 (B_1) antisymmetric stretch mode ($\sim 1275 \text{ cm}^{-1}$). (b) The point-group symmetry of an isotropic molecule is determined by its symmetry elements. A C_{2v} symmetry NO_2^- molecule (both oxygens the same isotope) has a twofold rotation axis C_2 taken as vertical (v) and two vertical reflection planes σ_v and σ_v' . A lower symmetry C_s molecule (two different oxygen isotopes) only has the σ_v reflection plane. The principle molecular axes are labeled A , B , and C by the convention that the moments of inertia satisfy $I_A < I_B < I_C$.

tions are determined by the symmetry of the molecule.⁵² The point-group symmetry of the bent NO_2^- molecule is C_{2v} when the oxygen isotopes are the same, or C_s when the oxygen isotopes are different. The symmetry elements of the C_{2v} molecule are shown in Fig. 4(b). The C_{2v} transition dipoles lie along the axes labeled A , B , and C . The A_1 symmetric modes ν_1 and ν_2 have transition-dipole moments that point along the B (C_2) axis. The ν_3 antisymmetric stretch mode has its transition dipole along the A axis (the O-O axis). (The ν_3 mode belongs to the B_1 representation. Note that depending upon which reflection plane is primed, different authors identify ν_3 with either the B_1 or the B_2 representation. We will adhere to the former convention.) For the lower-symmetry C_s molecules, the transition dipoles are only guaranteed by symmetry to lie in the plane of the molecule or perpendicular to it. The vibrational-mode transition dipoles must lie in the plane of the molecule. Since the oxygen mass difference is not large, these moments are probably close to the A and B axes, but not in them. The permanent dipole moment of the molecule points along the B axis.⁵³ Infrared absorption spectra of the three internal vibrational-mode fundamentals and the two strongest vibrational combination modes for the NO_2^- ion in KCl, KBr, and KI at 1.6 K have been measured at 0.03 cm^{-1} resolution with Bomem and Bruker interferometers.

1. Bending mode (ν_2)

A careful examination of the 800 cm^{-1} bending-mode region, shown in Fig. 5, reveals that the IR spectrum for the

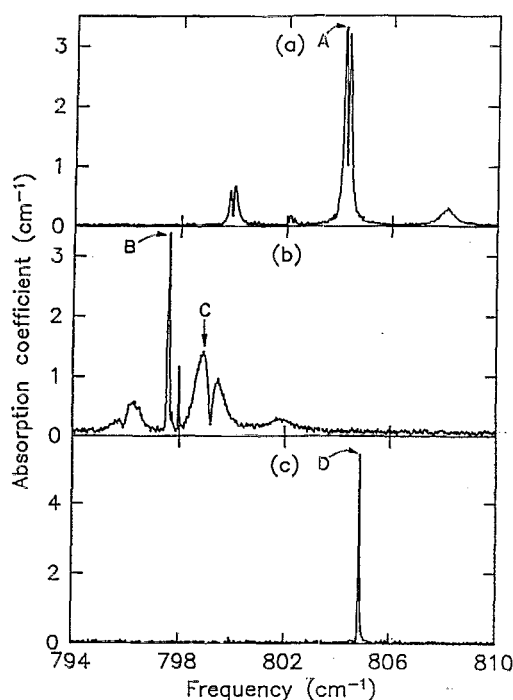


FIG. 5. Infrared ν_2 bending-mode absorption spectra of NO_2^- in potassium halide single crystals at 1.6 K. The measured concentrations in the three sample spectra are (a) KCl + 0.008 mole % NO_2^- , (b) KBr + 0.016 mole % NO_2^- , and (c) KI + 0.011 mole % NO_2^- . New spectral features are resolved for the sum and difference band tunneling structures in (a) KCl (14,16,16) and (b) KBr (14,16,16). (c) For KI: NO_2^- , no tunneling structure is observed. The sharp ν_2 bending mode is unresolved in (c) even at 0.03 cm^{-1} resolution (diode laser measurements give a concentration dependent full width at half maximum of 0.01 to 0.016 cm^{-1}). Capital letters A–D mark the frequencies at which persistent hole burning results will be referred to later in the text.

KI host is fundamentally different from that for KCl or KBr. An intricate and related structure is observed in the case of the KCl and KBr bending modes [Figs. 5(a) and 5(b)]. The sharp, pure vibrational ν_2 bending mode (or Q transition⁵⁴) is seen near Fig. 5(a) 802 cm^{-1} and 5(b) 797.6 cm^{-1} . (Weaker Q lines probably belong to associated impurity clusters, since they do not have the strong temperature dependence of the strongest Q lines). Broader, temperature-dependent sum and difference bands are also present about the Q region in Figs. 5(a) and 5(b). The (a) KCl and (b) KBr sum and difference doublet bands closest to the Q band appear similar. Earlier infrared studies^{26,28} did not reveal the detail shown here. In particular, note the asymmetric doublets near A and C in the top two panels of Fig. 5, previously unresolved and characterized as single broad features. In addition, the higher-frequency sum band has a corresponding difference band that appears between a few K and 25 K. The full widths of each of the bands in the ν_2 region in freshly cleaved samples of KCl and KBr are ~ 0.2 and $\sim 1.2 \text{ cm}^{-1}$, respectively. Figure 5(c) shows the very different KI: NO_2^- bending mode marked by D, which is sharp, structureless, and occurs at a higher frequency than would be extrapolated with increasing lattice constant from the spectra in Figs. 5(a) and 5(b). Diode laser spectroscopic

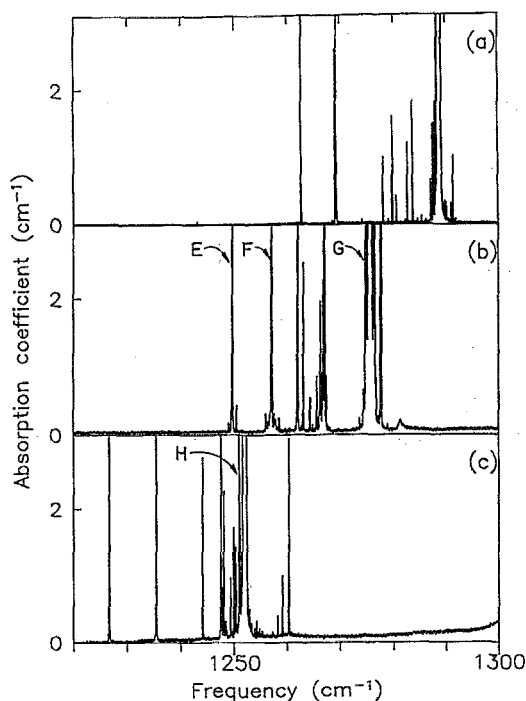


FIG. 6. Infrared ν_3 antisymmetric stretch mode absorption spectra of NO_2^- in potassium halide single crystals at 1.6 K. (Same samples and identification as used in Fig. 5.) The strongest vibrational absorption feature in each panel is the isolated (14,16,16) ν_3 mode with an absorption coefficient maximum far off scale. The lowest-frequency modes at (a) 1262.73 cm^{-1} , (b) 1249.75 cm^{-1} , and (c) 1226.64 cm^{-1} are for the much less abundant (15,16,16) isotope. For KCl and KBr, the (14,16,18) ν_3 mode consists of a doublet at (a) 1269.15 and 1269.37 cm^{-1} and (b) 1257.08 and 1257.15 cm^{-1} . The KI (14,16,18) ν_3 mode at 1235.40 cm^{-1} is a single sharp mode. Other lines in these spectra are for impurity clusters involving at least one (14,16,16) NO_2^- ion. Capital letters E–H mark the frequencies at which persistent hole burning results will be referred to later in the text.

measurements across this line show that it has a full width at half maximum (FWHM) of 0.01 to 0.016 cm^{-1} at 1.6 K, for concentrations of 10^{-4} – 10^{-2} mole %.

2. Antisymmetric stretch mode (ν_3)

The ν_3 antisymmetric stretch-mode region is shown in Fig. 6. A virtual forest of sharp lines with full widths on the order of 0.02 to 0.04 cm^{-1} are observed for each host crystal in Figs. 6(a), 6(b), and 6(c). They stem from isolated isotopically shifted NO_2^- defects, and for clusters of defects involving at least one NO_2^- ion. The exceptionally strong modes on the high-frequency end of each spectrum at Figs. 6(a) 1288.75 , 6(b) 1275.58 , and 6(c) 1252.03 cm^{-1} are the abundant (14,16,16) isotopic NO_2^- defect ν_3 modes. Since the (14,16,16) ν_3 mode is several hundred times stronger than other NO_2^- vibrational modes, a large number of lines belonging to lower concentration species can also be observed. Figure 6 emphasizes the ν_3 absorptions produced by other less abundant isotopes and defect pairs in lower concentration than the abundant (14,16,16) defect. Many of the lines have been identified with defect pairs involving $\text{NO}_2^-:\text{NO}_2^-$ (Refs. 31 and 32) molecules on near-neighbor

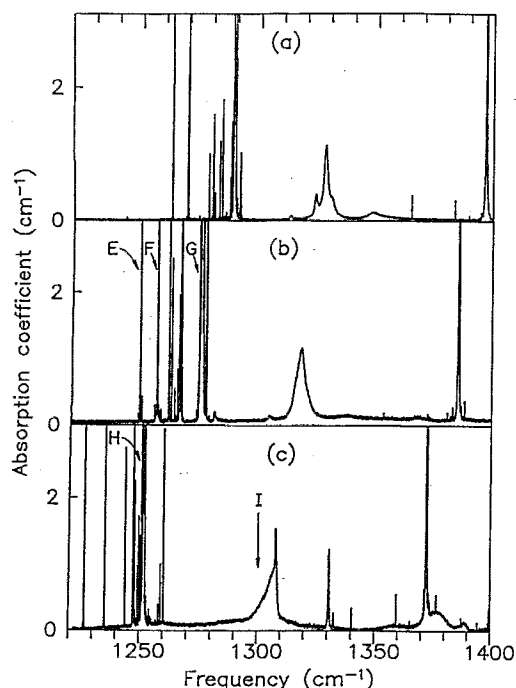


FIG. 7. Infrared ν_1 symmetric stretch-mode absorption spectra of NO_2^- in potassium halide single crystals at 1.6 K. (Same samples and identification as used in Fig. 5.) The ν_1 symmetric stretch mode in the 1300 to 1330 cm^{-1} region is within the combination spectrum of the ν_3 plus host phonon modes. (The strong ν_3 stretch modes for isotopes of the NO_3^- nitrate ion are also observed in the 1340 to 1400 cm^{-1} region.) For each host, the NO_2^- ν_1 modes have strikingly different mode widths and shapes. The peak frequencies are (a) 1325 cm^{-1} , (b) 1317 cm^{-1} , and (c) 1308 cm^{-1} . Additional lines for $\text{KI}:\text{NO}_2^-$ near 1330 cm^{-1} are phonon-gap-mode ν_3 sidebands. Capital letters E–I mark the frequencies at which persistent hole burning results will be referred to later in the text

anion sites. The two lowest-frequency ν_3 modes [e.g., E and F in Fig. 6(b)] belong to the isolated (15,16,16) and the (14,16,18) isotopic species with relative natural abundances of 0.37% and 0.41%, respectively.^{26,28} Notice that the tunneling structure coupled to the ν_2 (A_1) mode in Fig. 5 is not seen in the region of the ν_3 (B_1) mode in KCl and KBr in Fig. 6.²⁶

3. Symmetric stretch mode (ν_1)

The ν_1 (A_1) symmetric stretch-mode region (1300 to 1350 cm^{-1}) in Fig. 7 contains broad features for all three hosts. The sharp lines at lower frequencies are the same as those shown in Fig. 6. The symmetric stretch mode shows somewhat more structure in KCl and KBr than it does in KI [the region labeled I in Fig. 7(c)], a result somewhat similar to that observed for the ν_2 symmetric bending mode in Fig. 5. The tunneling-vibrational fine structure observed in the ν_1 mode in KCl and KBr shows widths ranging between 1.3 to 3.5 cm^{-1} . This result should be compared to the 0.2 and 1.2 cm^{-1} widths observed for the ν_2 mode. The ν_1 mode of NO_2^- in KI has an isotope-dependent asymmetric shape

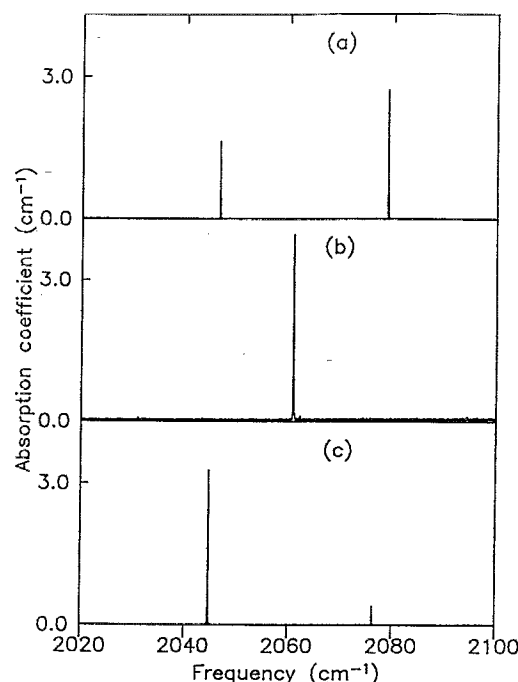


FIG. 8. Infrared $[\nu_2 + \nu_3]$ vibrational combination mode absorption spectra of NO_2^- in potassium halide single crystals at 1.6 K. (Same samples and identification as used in Fig. 5.) The sharp (14,16,16) $[\nu_2 + \nu_3]$ combination modes (with linewidths 0.06 to 0.07 cm^{-1} FWHM) are at (a) 2078.85 cm^{-1} in KCl, (b) 2060.93 cm^{-1} in KBr, and (c) 2044.86 cm^{-1} in KI. Additional lines seen in these spectra probably belong to (a) the $\text{KCl}:\text{B}^{16}\text{O}_2^-$ ν_3 mode (2046.52 cm^{-1}) and (b) the $\text{KI}:\text{NO}_3^-$ nitrate defect $[\nu_3 + \nu_4]$ mode (2076.31 cm^{-1}).

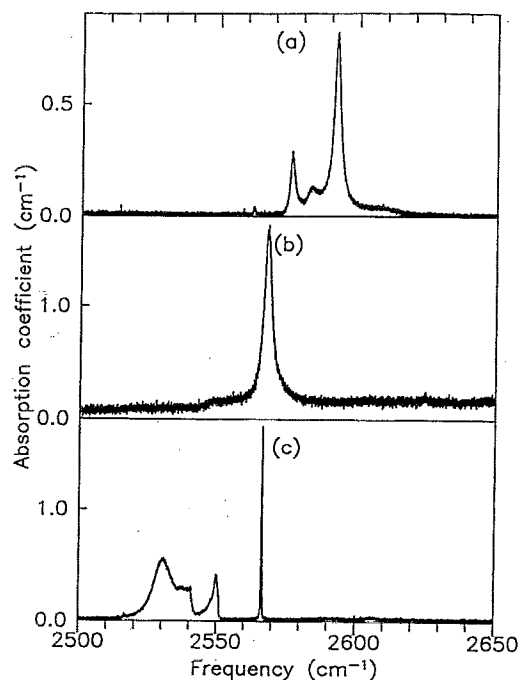


FIG. 9. Infrared $[\nu_1 + \nu_3]$ vibrational combination mode absorption spectra of NO_2^- in potassium halide single crystals at 1.6 K. (Same samples and identification as used in Fig. 5.) The structure in the 2500 to 2650 cm^{-1} region in each panel has been assigned to the NO_2^- $[\nu_1 + \nu_3]$ combination mode.

with a broad width of $\sim 3 \text{ cm}^{-1}$. $\text{KI}:\text{NO}_2^-$ also has relatively sharp side band modes near 1330 cm^{-1} that previously have been identified as combinations of $\nu_3 + \text{gap modes}$.²⁶ The strong sharp absorption line in the 1370 to 1400 cm^{-1} region is due to the ν_3 mode of the NO_3^- nitrate ion.^{14,26,28,55}

4. Overtone region

Figure 8 presents the spectra for the $[\nu_2 + \nu_3](B_1)$ overtone region from 2020 to 2100 cm^{-1} . This mode consists of a single sharp vibrational line with a FWHM of 0.06 to 0.07 cm^{-1} in all three hosts crystals. Again, note that the tunneling structure which is coupled to the A_1 internal modes is not observed for this B_1 mode frequency either for KCl or KBr.²⁶

The 2500 to 2650 cm^{-1} overtone region, shown in Fig. 9, contains the $\text{NO}_2^- [\nu_1 + \nu_3](B_1)$ combination mode. Little is actually known about the different structure shown in each of the panels, but it may involve tunneling motion in Figs. 9(a) KCl and 9(b) KBr or resonances with phonon side bands in combination with the much weaker $2\nu_3$ modes [which should occur near Figs. 9(a) $\sim 2570 \text{ cm}^{-1}$, 9(b) $\sim 2550 \text{ cm}^{-1}$, and 9(c) $\sim 2500 \text{ cm}^{-1}$].

5. Dislocation induced changes

While making high-resolution measurements in the bending-mode region it was observed that the widths of the

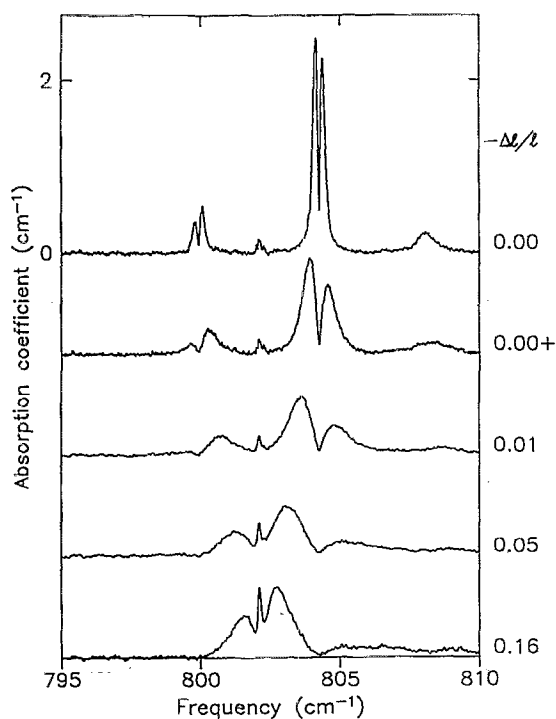


FIG. 10. Dependence of the $\text{KCl}:\text{NO}_2^- \nu_2$ absorption spectrum on dislocation defect density at 1.5 K . Samples were hot forged to produce permanent plastic deformations with strains $-\Delta l/l$ from 0 to 16% . At 1.5 K , these reorientational tunneling-vibrational combination modes broaden and the doublet peaks separate with strain. Notice that the absorption notch positions between the doublets at 799.93 and 804.25 cm^{-1} do not move to within $\pm 0.02 \text{ cm}^{-1}$.

tunneling sideband doublet structures in the $\text{KCl}:\text{NO}_2^-$ and $\text{KBr}:\text{NO}_2^- \nu_2$ regions resolved in Figs. 5(a) and 5(b) depend on the sample preparation history. Samples that were turned down on a lathe showed a broadening of the doublets because of the introduction of dislocations into the crystal.

To further investigate this dislocation broadening effect, a series of samples were prepared with different dislocation densities. Figure 10 shows the effect upon the $\text{NO}_2^- \nu_2$ doublets centered about 804 and 800 cm^{-1} of dislocations introduced into KCl crystals during forge hardening at 100°C . The final uniaxial pressures obtained during this process were between 300 and 800 atm producing permanent plastic deformations with strains $-\Delta l/l$ from 0% to 16% . Figure 10 shows that the peaks broaden and the peak frequencies of the doublets move apart with increased dislocation density; however, the V-notch minima between the peaks does not fill in. Instead, the absorption band still retains sharp minima positioned at 799.93 and 804.25 cm^{-1} . These V-notch frequencies are found to remain fixed to within an accuracy of $\pm 0.02 \text{ cm}^{-1}$. Such insensitivity to sample strains has turned out to make the notch a useful marker of the doublet position.

6. Summary of mode frequencies

The frequencies of the vibrational modes of NO_2^- ions in KCl, KBr, and KI at 1.6 K are listed in Table II. Most of the frequencies are selected at mode peaks, but the frequencies in parentheses are the absorption notch positions. The lowest sideband frequencies listed for ν_2 and ν_1 in Table II for KCl and KBr are observed for temperatures on the order of a few K to 25 K . All ν_3 modes have a single sharp absorption line, except for the lower symmetry (14,16,18) isotope in KCl and KBr. Here, the transition dipole moment does not lie along the O-O axis, and a sharp doublet is resolved that may be a coupling of the ν_3 mode to the reorientational tunneling modes for this isotope. The ν_1 mode for $\text{KI}:\text{NO}_2^-$ is a single broad asymmetric feature for the C_{2v} symmetry molecules. However, for the lower C_s symmetry (14,16,18) isotopic molecule, an 8 cm^{-1} doublet is observed. The lower symmetry of the (14,16,18) molecule allows both components of the ν_1 doublet observed in Raman scattering for the (14,16,16) C_{2v} symmetric molecule to become infrared active.

B. NO_2^- persistent infrared hole burning results

PIRSH burning has been attempted in all of the isolated NO_2^- defect vibrational-mode fundamentals for some isotopic combination in KCl, KBr, and KI, and for the overtone transition ($\nu_2 + \nu_3$) in KCl and KI. NO_2^- persistent spectral hole burning is found to occur in each of these host crystals. An identification of modes which showed burning and those that did not has been made in Table II where a Y (yes) or N (no) superscript has been attached to the appropriate vibrational mode frequency. All attempts at infrared hole burning in KI yield some sort of persistent spectral change for sufficiently high intensity. As seen in Table II, not all NO_2^- infrared modes in KCl and KBr could be hole

TABLE II. Vibrational-mode frequencies (in cm^{-1}) for NO_2^- defects in crystals at 1.6 K. We find that PIRSH burning is possible in modes labeled with a Y. An absence of PIRSH burning is noted for modes labeled with an N. *P*, *Q*, and *R* are fine structure labels for the ν_2 and ν_1 vibrational modes.

Host crystal	Defect isotope	Vibrational mode				
		ν_2	ν_3	ν_1	$(\nu_2 + \nu_3)$	$(\nu_1 + \nu_3)$
KCl	(14,16,16)	796.43 <i>P</i> (2)	1288.75	1320.0	2078.85 ^N	2562.5
		799.76 ^Y <i>P</i> (1 ⁻)				2576.2
		(799.93) <i>P</i> (1)		1323.77		2583.3
		800.11 ^Y <i>P</i> (1 ⁺)				2592.16
		802.10 ^Y <i>Q</i>		1325.7 ^a		2608.7
		804.08 ^Y <i>R</i> (0 \rightarrow 1 ⁻)				
		(804.25) <i>R</i> (0 \rightarrow 1)		1327.9 ^N		
		804.40 ^Y <i>R</i> (0 \rightarrow 1 ⁺)				
		808.15 ^N <i>R</i> (1)		1330.70 ^N		
	(14,16,18)		1269.15 ^Y			
	(15,16,16)		1269.37 ^Y			
	(14,16,16)	793.45 <i>P</i> (2)	1275.58 ^Y	1312.9	2060.93	2548.2
	795.67 <i>P</i> (1 ⁻)			2567.95		
	(795.90) <i>P</i> (1)	1315.5				
796.25 <i>P</i> (1 ⁺)						
797.51 <i>Q</i>						
797.61 ^Y <i>Q</i>	1316.9					
798.91 <i>R</i> (0 \rightarrow 1 ⁻)						
(799.20) <i>R</i> (0 \rightarrow 1)	1318.42 ^N					
799.45 ^Y <i>R</i> (0 \rightarrow 1 ⁺)						
(14,16,18)	801.78 ^N <i>R</i> (1)	1321.05				
KBr	(14,16,18)		1257.08 ^Y			
	(15,16,16)		1257.15 ^Y			
	(14,16,16)	804.85 ^Y	1252.03 ^Y	1308.0 ^Y	2044.86 ^Y	2530.4
						2540.63
						2549.95
						2566.53
						2449.74
						2506.84
						2516.67
						2530.68
	(15,16,16)	799.93 ^Y				
	(14,18,18)	766.65 ^Y	1225.96	1272.3	1981.12	2473.13
						2488.62
						2494.23
					2512.91	
KI	(15,16,18)		1209.60			
	(15,18,18)		1199.90			

^aThis *Q* branch is revealed under uniaxial stress.

burned using the maximum intensity provided by our diode lasers.

1. $\text{KI}:\text{NO}_2^-$ hole burning

Figure 11 shows the PIRSH burning effects that can be produced with a low-power diode laser in the single narrow line associated with the ν_2 (A_1) infrared bending mode of NO_2^- at 804.85 cm^{-1} .⁴⁴ Figure 11(a) shows the unaltered absorption band as measured in transmission by tuning the attenuated laser frequency through a few GHz about the line center. To burn a hole, the laser frequency is returned to the center of the absorption band and then held fixed. At the highest intensities used (25 mW/cm^2) the absorption at the laser frequency decreases to zero in about 10 s. In the dark (beam blocked), this absorption hole decays roughly exponentially with a decay time of $\tau = 50 \text{ min}$ at 1.5 K. Placing

cold interference filters on the sample so that broad band blackbody thermal radiation from the room can only excite the ν_2 bending mode does not alter the hole decay time.

The persistent hole shown in Fig. 11(b) is 200 MHz wide because it is essentially 100% deep. Holes as narrow as 37 MHz have been burned in this band in the low intensity, short burn time limit. The combination of the total integrated absorption strength of the bending mode, the concentration of defects, and the homogeneous linewidth found through hole burning gives a lower limit on the ν_2 mode peak cross section $\sigma = 2.1 \times 10^{-16} \text{ cm}^2$.

Since the dipole moment of this bending mode is parallel to the permanent dipole moment of the symmetric molecule, it has been possible, by studying the polarization properties of the persistent holes, to determine that for this host, the O-O axis of this molecule is directed along the $\langle 110 \rangle$ crystal

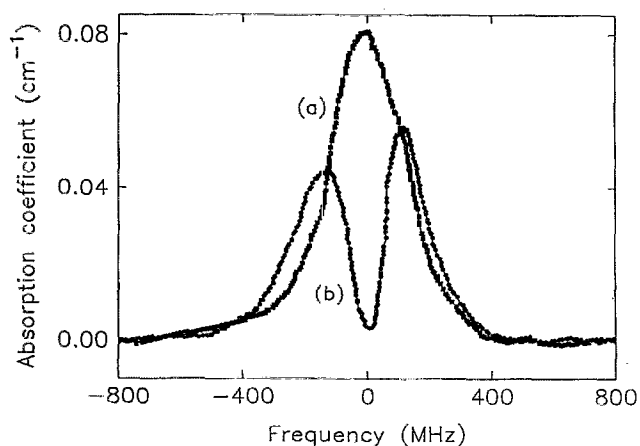


FIG. 11. Demonstration of PIRSH production for the ν_2 mode in $\text{KI}:\text{NO}_2^-$. An example of a persistent hole burned in the 804.85 cm^{-1} infrared bending-mode absorption of $\text{KI} + 0.000\,11$ mole % NO_2^- at 1.5 K . The spectrum is shown (a) before and (b) after hole burning. Note that 37% of the absorption strength removed at the laser burn frequency has appeared in the wings in the same polarization. This absorption line is marked with a *D* in Fig. 5 (after Ref. 44).

axes and the permanent dipole moment of the molecule is oriented along the $\langle 100 \rangle$ crystal axes.^{44,45}

At 1.5 K the quantum efficiency η for burning a hole is found from the initial slope of a transmission growth curve and the peak cross section to be $\eta \approx 10^{-2}$. In other words, roughly 1 in 100 absorbed photons per defect causes an NO_2^- molecule with mode centered at the laser frequency to be hole burned.

It is observed that 100% deep holes are only possible within a certain range of laser intensity and sample temperature. Holes burned with an intensity of 0.2 mW/cm^2 are only

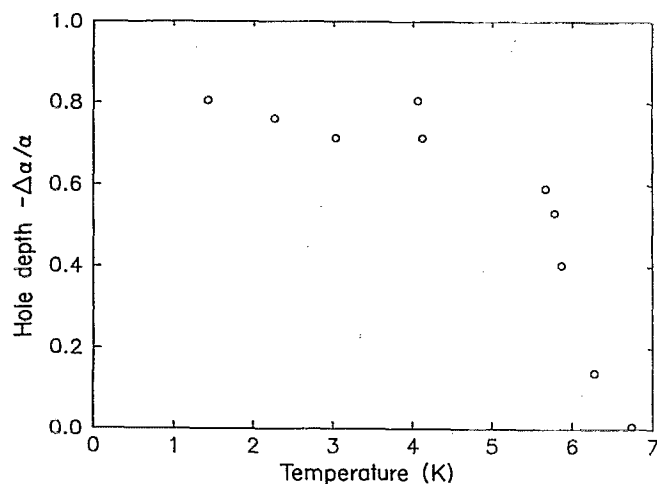


FIG. 12. Temperature dependence of the asymptotic hole depth for the ν_2 mode in $\text{KI}:\text{NO}_2^-$. At an intensity of 0.2 mW/cm^2 and temperature of 1.5 K , an initial $\text{KI}:\text{NO}_2^-$ ν_2 absorbance of $\alpha_0 l = 1.0$ ($l = 0.079\text{ cm}$) is burned away to an equilibrium hole depth of $-\Delta\alpha/\alpha_0 = 0.8$. The asymptotic hole depth at higher temperatures remains roughly constant up to about 5 K and then decreases rapidly between 5 and 7 K . No hole burning is observed above 8 K .

burned 80% deep (for $l = 0.079\text{ cm}$ and $\alpha_0 l = 1.0$), and no detectable hole is burned with an intensity less than $2\text{ }\mu\text{W/cm}^2$ at 1.5 K .⁴⁴ In other words, there is a minimum intensity below which the long time hole depth decreases.

The temperature dependence of the hole depth for the bending mode is shown in Fig. 12. The asymptotic equilibrium hole depth at an intensity of 0.2 mW/cm^2 is roughly constant up to 5 K , and then decreases as the temperature is raised to 7 K . The hole relaxation time also decreases with increasing temperature above 5 K . Detectable holes are not produced above 8 K , and holes burned at lower temperatures are rapidly erased by warming the crystal above 8 K . Clearly, this type of vibrational hole burning is a low temperature effect.

Persistent changes can also be produced in the higher frequency ν_3 mode and also in the $[\nu_2 + \nu_3]$ combination band with different diode lasers. Figure 13 compares the spectrum for the wing of the strongly absorbing asymmetric ν_3 mode as measured by Fig. 13(a) an FT interferometer and Fig. 13(b) a diode laser. The interferometer barely resolves the collection of closely spaced lines which are identified by the letter *H* in Figs. 6 and 7. The lines appear resolved in the diode laser scan.

Locating the same absorption wing with the diode laser as with the interferometer is accomplished by first coarse temperature tuning the diode laser and coarse filtering the laser with a monochromator for rough frequency calibra-

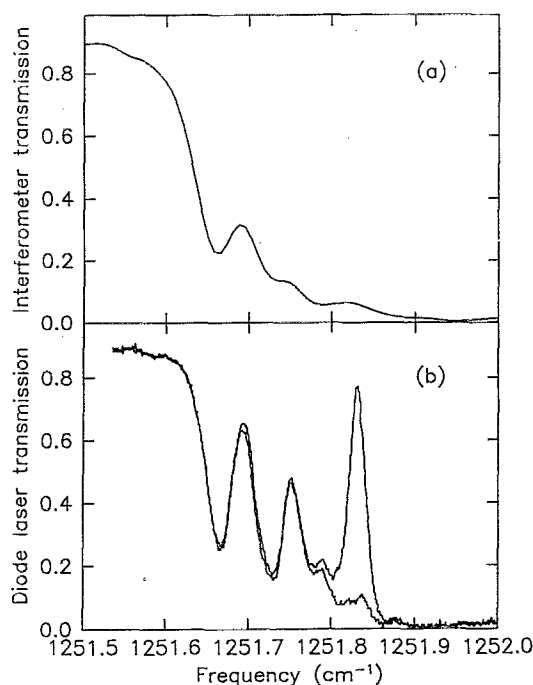


FIG. 13. Example of a PIRSH produced in the low-frequency wing of the $\text{KI} (14,16,16)\text{ }\nu_3$ absorption band. Transmission spectra taken with (a) an interferometer (0.03 cm^{-1} resolution) and (b) a diode laser are compared for the low-frequency wing of the very strongly absorbing ν_3 band centered at 1252.03 cm^{-1} . In (b), two traces are shown, one before and one after a hole is burned at 1251.83 cm^{-1} . This region is identified with an *H* in Figs. 6 and 7. The sample is a 0.079 cm thick slab of $\text{KI} + 0.02$ mole % NO_2^- at a temperature of 1.6 K .

tion. Fine-frequency identification is performed by comparing the observed diode laser spectrum with the previously recorded interferometer spectrum.

To burn the hole shown in Fig. 13(b) the diode frequency is fixed near 1251.83 cm^{-1} for a few tens of seconds. The recording of a second diode laser spectrum reveals a deep absorption hole at the laser burn frequency. In this example, the hole is saturation broadened. PIRSH's can be produced anywhere in the wings of this strong (14,16,16) isotopic $\text{NO}_2^- \nu_3$ pair mode region. Burning holes in the low-intensity short burn time limit produces holes of 60 MHz width. The sharp higher-frequency $[\nu_2 + \nu_3]$ combination band gives PIRSH's with a width of 500 MHz (FWHM). These hole widths are qualitatively similar to those observed for other vibrational defects (10 MHz for ReO_4^- and 50 MHz to 500 MHz for CN^- in alkali halide crystals).⁵⁶

A different kind of persistent effect is shown in Fig. 14 where burning anywhere in the broad ν_1 symmetric stretch mode alters the entire band, in contrast to the narrow holes found for the narrow ν_2 and ν_3 modes. The sample transmission in the ν_1 mode region is observed to increase over a few minutes period when the diode laser frequency is held anywhere within the triangular shaped absorption band. Sweeping the diode laser frequency over its maximum current tuning range of about 0.6 cm^{-1} after the sample transmission has increased, does not reveal a persistent hole, hence, the

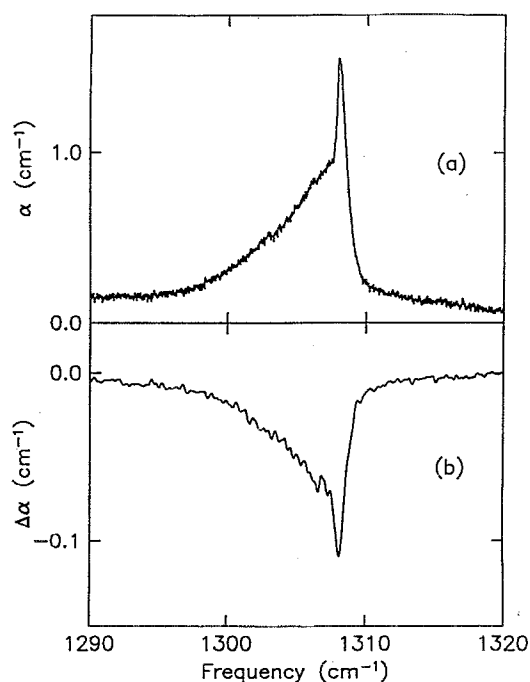


FIG. 14. The very broad persistent spectral change produced in the $\text{KI}:\text{NO}_2^- \nu_1$ symmetric stretch mode region. (a) The absorption coefficient for $\text{KI} + 0.011 \text{ mole } \% \text{ NO}_2^-$ taken with an interferometer (0.03 cm^{-1} resolution) at 1.6 K. This mode is identified by an I in Fig. 7. (b) The change in absorption coefficient $\Delta\alpha$ (resolution 0.25 cm^{-1}) that is produced with diode laser light at 1307.2 cm^{-1} with laser polarization along a $[100]$ crystal axis, perpendicular to the unpolarized interferometer beam axis. Burning with the diode laser frequency down on the wing at 1304.2 cm^{-1} or above the peak at 1308.7 cm^{-1} produces a similar change.

persistent absorption change is much larger than 0.6 cm^{-1} in width. Exposing a large volume of the sample to diode laser light with the laser frequency held fixed within the ν_1 mode for about a half hour produces a spectral change which can be measured with the interferometer: The entire 3 cm^{-1} (90 GHz) wide triangular shaped ν_1 band decreases uniformly in strength, as illustrated in Fig. 14(b). This result is in marked contrast with the narrow holes produced in the ν_2 , ν_3 , or $[\nu_2 + \nu_3]$ bands.

To insure that spectral diffusion among the defects is not responsible for the apparently broad ν_1 mode change during the hole burning process, we have probed the polarization properties of the absorption change. If the very broad spectral change is due to rapid energy transfer occurring on a time scale much shorter than the hole burning in an inhomogeneous band, then the change should appear unpolarized in a cubic crystal. However, it is observed that burning this ν_1 mode with the laser beam polarized in a $[100]$ crystal direction produces a $[100]$ polarized change in absorption. Hence, intermolecular vibrational energy transfer is not responsible for the change in the entire mode strength of Fig. 14. Our conclusion is that this unusually shaped band is homogeneously broadened.

2. Hole burning attempts on ν_1 , ν_3 , and $[\nu_2 + \nu_3]$ in $\text{KBr}:\text{NO}_2^-$ and $\text{KCl}:\text{NO}_2^-$

Similar persistent burning effects have been found for both KCl and KBr host crystals. In contrast with the $\text{KI}:\text{NO}_2^-$ data reported in the preceding subsection no hole burning has been detected for the broad ν_1 modes and for the $[\nu_2 + \nu_3]$ combination band at an intensity of 25 mW/cm^2 . However, persistent effects have been observed for the sharp ν_3 stretch mode and these are presented here.

PIRSH's can be produced in the ν_3 modes of the (14,16,16;), (15,16,16), and (14,16,16), NO_2^- isotopic defects in KBr . Burning has been carried out at the three frequencies labeled E , F , and G in Figs. 6 and 7. Figure 15 shows that persistent holes are produced in the ν_3 mode with full widths at half maxima of 300 to 400 MHz. In Fig. 15(a), a hole burned on the low-frequency wing of the $\text{KBr}:\text{NO}_2^- \nu_3$ mode, labeled 0 GHz (at position G in Figs. 6 and 7) produces an antihole located at lower frequency ($\sim 3 \text{ GHz}$) than the hole. As previously noted for $\text{KI}:\text{NO}_2^-$, the wing of the abundant (14,16,16) isotope ν_3 band is composed of many individual lines, probably associated with different types of defect clusters. Burning a hole in one of these lines causes an antihole line to appear at a particular frequency shifted from the hole. This finding is similar to that previously observed for CN^- impurity clusters in KBr .^{57,58}

The spectra shown in Fig. 15(b) indicate that the lower symmetry (14,16,18) ν_3 mode produces a doublet structure. The hole burned at 0 GHz (at position F in Figs. 6 and 7) does not produce a hole in the other component of the doublet shifted by 1.2 GHz. It is observed that holes can be burned in either of the components of the doublet with no major effect on the other aside from a small increase in the strength of the doublet away from the laser burn frequency. As in Fig. 15(c), only weak holes are produced in the ν_3

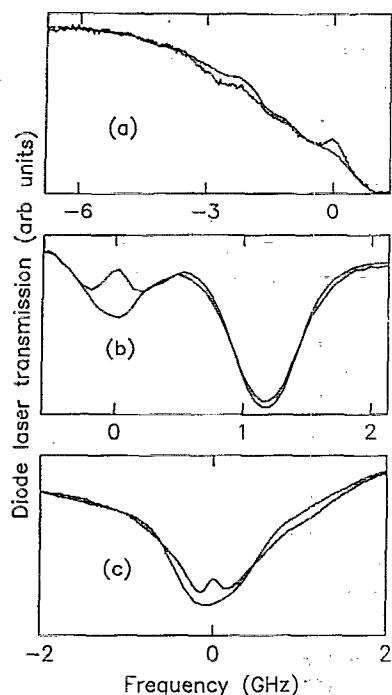


FIG. 15. PIRSH's produced in the ν_3 modes of the abundant (14,16,16) and less abundant (15,16,16) and (14,16,18) isotopic NO_2^- defects in KBr. For each isotopic NO_2^- defect ν_3 mode in samples of KBr + 0.02 mole % NO_2^- at 1.6 K, two diode laser signal traces are obtained before and after a hole is burned at position O on the frequency axis. (a) a PIRSH produced on the low-frequency wing of the very strong (14,16,16) isotope ν_3 mode near 1275.5 cm^{-1} also results in an antihole localized a few GHz lower than the hole. This region is marked with a G in Figs. 6 and 7. (b) Holes may be produced in either of the doublets: $\nu_3 + \text{tunneling}$ mode for this lower symmetry (14,16,18) isotopic defect mode near 1257.1 cm^{-1} . This region is marked with an F in Figs. 6 and 7. (c) Holes are also produced in the (15,16,16) isotopic defect ν_3 mode at 1249.75 cm^{-1} . This mode is marked with an E in Figs. 6 and 7.

mode with laser polarization in a $[100]$ crystal direction for the (15,16,16) symmetric defect. Initially no hole burning was observed for the KCl (15,16,16) ν_3 mode with $[100]$ laser burn polarization; however, with the polarization in a non- $\langle 100 \rangle$ direction, holes have been produced.

All attempts to burn holes in the very broad ν_1 structures in KCl and KBr have failed. No detectable persistent spectral changes occur with diode intensities of $\sim 25 \text{ mW/cm}^2$ and laser burn polarizations in $\langle 100 \rangle$ crystal directions. An attempt to hole burn the $[\nu_2 + \nu_3]$ combination band of KCl:NO_2^- with laser burn polarization in a $[100]$ crystal direction also failed. Because different polarizations have not been tried, it is not definitely known whether or not these modes show persistent effects. However, a comparison of the hole burning intensities for the ν_2 modes of NO_2^- in KCl, KBr, and KI to be presented in Sec. V A indicates that the diode intensity is simply not large enough for these broader modes.

3. Hole burning the ν_2 mode in KCl:NO_2^- and KBr:NO_2^- : Infrared satellite holes

Here the first observation of persistent multiple satellite holes in an infrared vibrational band at frequencies away

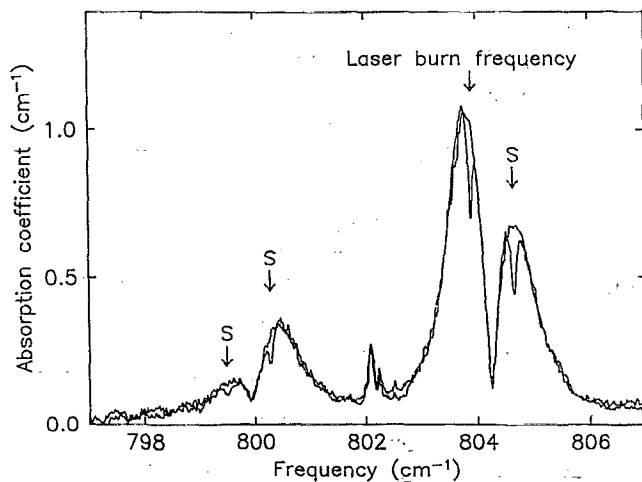


FIG. 16. Nonresonant satellite holes in the bending-mode absorption spectrum of KCl:NO_2^- at 1.6 K. The nitrate concentration is 0.012 mole %. Two interferometer traces are shown at the 0.03 cm^{-1} resolution; before and after a hole is burned with a diode laser at a burn frequency of 803.91 cm^{-1} . The unburned spectrum consists of sharp central Q features near 802 cm^{-1} and a sum and difference band doublet. The burned spectrum not only contains the sharp hole burned at the diode laser frequency (803.91 cm^{-1}), but also has three other satellite holes labeled by an S in each of the sum and difference modes. The laser burn frequency is marked with an A in Fig. 5.

from the laser burn frequency is presented. To investigate under what conditions of inhomogeneous broadening satellite holes can be observed in a vibrational mode, temperature and uniaxial stress dependence of the KCl:NO_2^- and KBr:NO_2^- absorption spectra also have been obtained.

Figure 16 shows two interferometer traces of the complex KCl:NO_2^- absorption spectrum in the ν_2 bending mode region before and after a hole has been burned at 803.91 cm^{-1} . (This frequency location is identified by the arrow A in Fig. 5. The doublets straddling the notches near 804 and 800 cm^{-1} in this figure are strain broadened, as the single-crystal sample was turned down to a 2.5 mm diameter rod.) Sharp satellite holes (S) appear in the absorption band on both sides of the V-shaped notch. The widths of the holes are all 0.75 GHz as measured with the diode laser. The observed multiplicity of holes means that when a single defect burns, four lines in the ν_2 fine structure belonging to that defect change. The equal hole widths imply that inhomogeneous broadening in one band is highly correlated inhomogeneous broadening in the others. Since the holes are correlated, these complex V-notched absorption bands are all associated with transitions belonging to a single defect type, a result very different from that found for the ν_3 mode described earlier. This strong correlation of center frequencies in different inhomogeneously broadened absorption peaks has only been observed within the ν_2 vibrational mode for KCl:NO_2^- . [The corresponding combined FTS diode laser hole burning experiment for the much more difficult to burn KBr:NO_2^- system has not been attempted. Also, it should be mentioned that the broader ν_2 sidebands at 808.15 cm^{-1} in KCl:NO_2^- and 801.78 cm^{-1} in KBr:NO_2^- do not hole burn

(see Figs. 5(a) and 5(b) and Table II).]

It is now evident that the unburned spectrum in Fig. 16 has a shape reminiscent of that observed in vibrational-rotational spectra with P , Q , and R components (labeling from lower frequency to higher).⁵⁴ The sharp central Q -like feature occurs near 802 cm^{-1} and sum (R) and difference (P) bands that contain the V-shaped notches near 804 and 800 cm^{-1} . Note that the P and R bands are not composed of numerous overlapping rotational-vibrational transitions for individual defects, but that each consists of an inhomogeneously broad single transitions for many defects.

The strong correlation of the burned hole and a satellite for a notched R band of the $\text{KCl}:\text{NO}_2^- \nu_2$ vibrational mode is presented in Fig. 17. Absorption coefficient traces obtained both before and after a hole has been burned on the low-frequency mode are shown overlayed on the left side of Fig. 17. The differences in absorption coefficient are shown on the right side. For each row of Fig. 17, a laser burn frequency has been selected within the low-frequency mode (marked with an A in Fig. 5), and absorption coefficient traces are obtained before and after a persistent hole is burned with the laser. From one row to the next, the previous hole is erased by thermal cycling to 20 K , and a new hole is burned at a lower frequency. Note that as the laser burn frequency is moved away from the notch position, the satellite hole also moves away. Burning holes in any of the other three modes shown in Fig. 16 shows a similar movement of the satellite

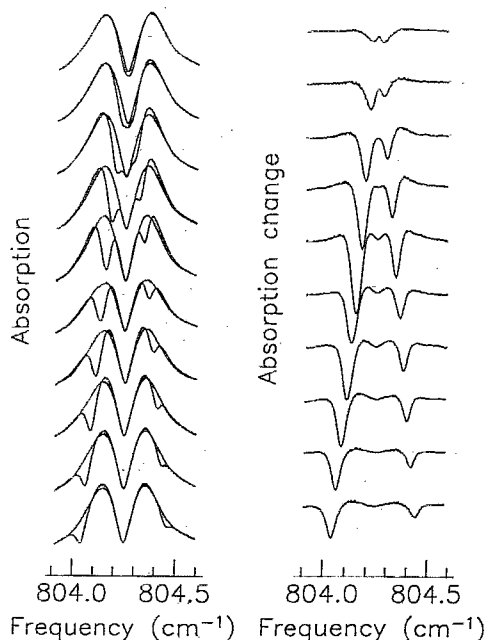


FIG. 17. Laser burn frequency dependence for a $\text{KCl}:\text{NO}_2^- \nu_2$ tunneling sideband persistent hole and satellite hole. Diode laser traces are shown for the $\text{KCl}:\text{NO}_2^- 804.25\text{ cm}^{-1} \nu_2$ tunneling sideband doublet at 1.6 K . Absorption coefficient traces obtained both before and after a hole has been burned on the low-frequency mode are shown overlayed on the left side of the figure. The differences in absorption coefficient are shown on the right side of the figure. Note that as the laser burn frequency is decreased, the corresponding satellite hole in the high-frequency mode moves to higher frequencies.

holes. Thus, these systematic hole burning experiments reveal that inhomogeneous broadening within the 804 and 800 cm^{-1} doublets occurs through a splitting of transitions centered about the 804.25 cm^{-1} and 799.93 cm^{-1} notch frequencies.

Figure 18 shows examples of the holes that are produced with an infrared diode laser in the $\text{KBr}:\text{NO}_2^- \nu_2$ bending mode region. Figures 18(a) and 18(b) each contain two raw signal traces for diode laser light transmitted through a sample doped with $0.02\text{ mole \% NO}_2^-$ at 1.6 K . One trace is recorded before a hole is burned, and another is recorded after burning for several minutes with the laser frequency held fixed at 0 on the frequency axis. Hole widths of roughly 0.35 and 1 GHz are produced in the Q -like and R -like regions. (The burn frequencies are identified by B and C in Fig. 5.)

The persistent holes generated both in KCl and $\text{KBr}:\text{NO}_2^-$ are more difficult to produce than those in $\text{KI}:\text{NO}_2^-$. These holes require a burn time of a few minutes to achieve a significant hole depth with intensities of $\sim 25\text{ mW/cm}^2$. Even with this longer burn time only shallow broad holes are produced in $\text{KBr}:\text{NO}_2^-$, and these have a short decay time of $\tau = 0.5\text{ min}$ at 1.5 K . In KCl , this maximum available intensity is just enough to produce holes that are nearly 100% deep with a longer decay time of $\tau = 15\text{ min}$ at 1.5 K . Estimates for the quantum efficiency of $\text{KBr}:\text{NO}_2^-$ and $\text{KCl}:\text{NO}_2^- \nu_2$ PIRSHs based on the fraction of the defects burned at the laser frequency and the burn fluence

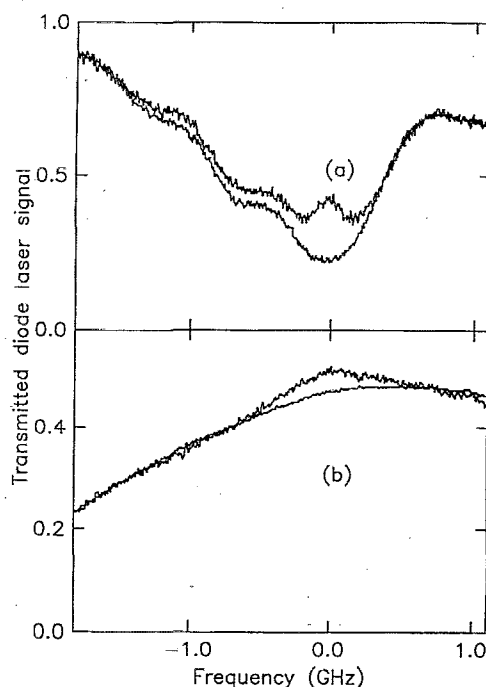


FIG. 18. PIRSH's produced in the $\text{KBr}:\text{NO}_2^- \nu_2$ bending mode and $\nu_2 +$ tunneling mode sidebands. (a) Example of hole production in the pure ν_2 bending mode or Q transition at 797.61 cm^{-1} . This mode is marked by B in Fig. 5. (b) Example of the broader hole that is produced in the $[\nu_2 + \text{tunneling mode}]$ sum band near 799.45 cm^{-1} . This mode is marked by C in Fig. 5.

(energy/cm²) gives $\eta \sim 10^{-4}$ which is 2 orders of magnitude smaller than for $\text{KI}:\text{NO}_2^-$.

4. Temperature dependence of the ν_2 reorientational tunnelling fine structure

Figure 19 shows the temperature dependent ν_2 absorption spectra for a freshly cleaved sample of $\text{KCl}:\text{NO}_2^-$. The pure vibrational (Q) transition is located in the middle of Fig. 19 at 802.10 cm^{-1} . Sum and difference bands are observed about the Q region. The absorption bands are observed to strictly increase, increase then decrease, and strictly decrease in integrated absorption strength with temperature from 1.7 to 15 K. The largest features at 1.7 K, namely the pair of R transitions summed on the Q near 804.25 cm^{-1} , strictly decrease in integrated absorption strength as the temperature is raised indicating that they originate from the ground state. The corresponding P difference doublet at 799.93 cm^{-1} and the broader R sum feature at 808.15 cm^{-1} both increase in integrated absorption strength from 1.7 to about 7 K and then decrease in strength at higher temperatures. The P difference band at 796.43 cm^{-1} increases in strength throughout the 1.7 to 15 K region. Between 15 and 25 K, these modes broaden and overlap into one broad absorption feature.

Figure 20 shows the temperature-dependent ν_2 absorption spectra for freshly cleaved $\text{KBr}:\text{NO}_2^-$. The pure vibrational Q region between 797 and 798 cm^{-1} contains four sharp lines at 0.03 cm^{-1} resolution. Two Q lines at 797.51

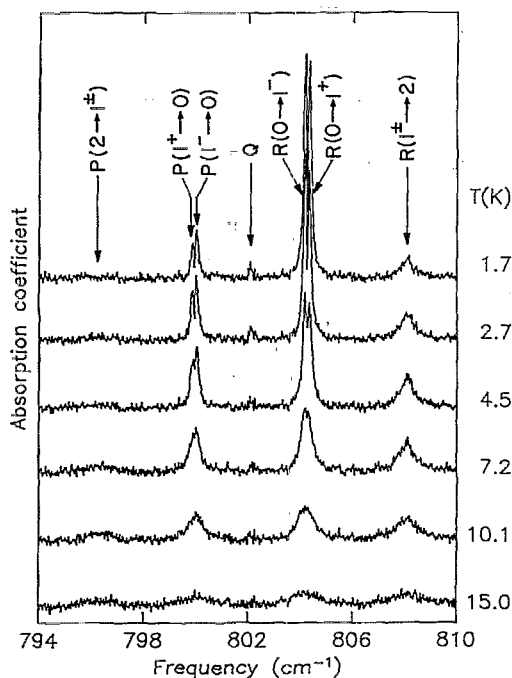


FIG. 19. Temperature dependence of the $\text{KCl}:\text{NO}_2^-$ ν_2 absorption spectrum. The interferometer resolution is 0.03 cm^{-1} . The dopant concentration is (nominally) $0.05 \text{ mole } \%$ NO_2^- . The sample temperature ranges between 1.7 and 15 K as given along the right ordinate. Modes are labeled with P , Q , or R , as described in the text.

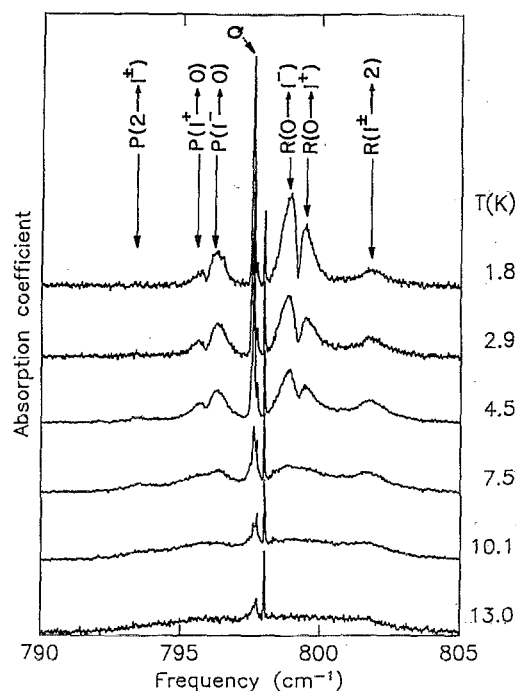


FIG. 20. Temperature dependence of a $\text{KBr}:\text{NO}_2^-$ ν_2 absorption spectrum. Interferometer resolution is 0.03 cm^{-1} . The dopant concentration is 0.016% NO_2^- . The sample temperature ranges between 1.8 and 13.0 K as given along the right ordinate. Modes are labeled with P , Q , or R , as described in the text.

and 797.61 cm^{-1} are not temperature dependent below 13 K. The R sum and P difference bands about the Q region have temperature-dependent behavior similar to that observed for $\text{KCl}:\text{NO}_2^-$ (see Fig. 19).

When the logarithmic ratios of the integrated absorption strengths of various band components are taken relative to the strongest R sum band for both Figs. 19 and 20 and plotted against $1/T$, it is found that the P -like lines originate from low-frequency Boltzmann populated levels. These levels are grouped 2 ± 0.5 and $8 \pm 0.5 \text{ cm}^{-1}$ from the ground state for $\text{KCl}:\text{NO}_2^-$ and 2 ± 0.5 and $6 \pm 0.5 \text{ cm}^{-1}$ from the ground state for $\text{KBr}:\text{NO}_2^-$.

The experimental energy-level diagram constructed from these hole burning and FTS experiments is given in Fig. 21. Our approach in constructing this diagram is similar to that of Avarmaa and Rebane,^{7,13} where the starting point is from experimental data rather than from assumed potential models. Hence, the one-dimensional rotor notation of Avarmaa and Rebane⁷ is used to characterize the spectrum. This notation is also shown in Figs. 19, 20, and 21. The one-dimensional rotor levels are labeled by a quantum number K' and K in the excited and vibrational ground states, respectively. Transitions are labeled with $P(K)$, Q , or $R(K)$, where P indicates $K' < K$ and R indicates $K' > K$. The temperature dependence described above is sufficient to locate the 2 cm^{-1} levels, represented by the dashed transitions in Fig. 21. Persistent infrared hole burning reveals that inhomogeneous broadening of the $P(1)$ and $R(0)$ bands is described by a transition splitting (Fig. 17), and it remains to determine

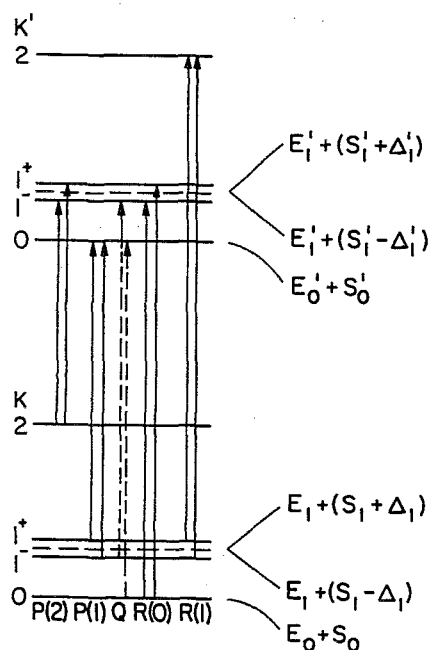


FIG. 21. Reorientational tunneling level diagram for NO_2^- ions in KCl and KBr crystals. Tunneling energy levels of NO_2^- in the ground and symmetric ν_1 and ν_2 vibrational states are shown consistent with experiment. The energy levels are labeled by a rotational quantum number K or K' in the vibrational ground or excited states. The dashed levels represent the unstrained and unsplit positions, the strain split levels are labeled by 1^- and 1^+ . Movement of the levels with strain is shown along the right side of the figure and described in the text.

which of the K or $K' = 0$ or 1 levels are split.

To determine which of the levels split to produce the V-shaped notches, the temperature dependence of a plastically deformed KCl: NO_2^- sample with a much greater splitting of the $P(1)$ and $R(0)$ doublets has been measured. Figure 22 shows the experimental results for a freshly cleaved crystal hot forged at 100°C with 30 MPa (300 atm) to a final deformation of about 1%. The Q band at 802.1 cm^{-1} is bracketed by sum and difference tunneling sidebands that are broadened by the increased crystal dislocation defect density. The $R(0)$ sum and $P(1)$ difference doublets with notches fixed at 804.25 and 799.93 cm^{-1} are broadened with

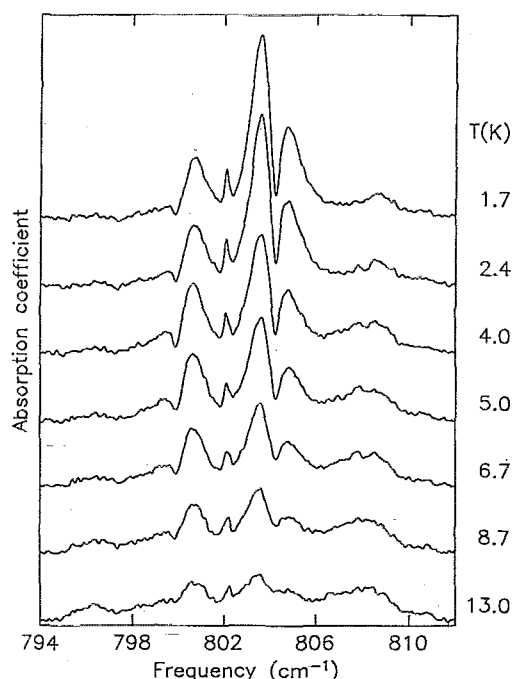


FIG. 22. Dependence of the KCl: NO_2^- ν_2 absorption spectrum temperature dependence on hot forging. Interferometer resolution is 0.12 cm^{-1} . The nitrite concentration is 0.04 mole % NO_2^- . The temperature is varied from 1.7 to 13 K as shown along the right ordinate.

the peak separation increasing from 0.3 in the undeformed to 0.7 cm^{-1} in the 1% deformed crystal. The strong $R(0)$ doublet at 804 cm^{-1} shows no change in the relative strengths of its lines with temperature; hence, the splitting for the $R(0)$ transition occurs in the $K' = 1$ level of the vibrationally excited state (see Fig. 21). The $P(1)$ doublet at 800 cm^{-1} does show relative strength changes in its two components, consistent with a $K = 1$ vibrational ground-state level splitting. The 808 cm^{-1} $R(1)$ sum band broadens to the low side, which is also consistent with a large $K = 1$ splitting in the deformed sample. Hence, the level splitting giving rise to the doublets is represented correctly by the pair of levels about the dashed unsplit $K = 1$ levels in Fig. 21. The values of the $K, K' = 1^\pm$ energies listed in Table III are obtained from the average peak splittings observed in the ν_2

TABLE III. Reorientational tunneling energies for KCl: NO_2^- and KBr: NO_2^- in vibrational ground and excited states (in cm^{-1}). Energies in parentheses correspond to the unstrained and unsplit notch frequencies in the $P(1)$ and $R(0)$ ν_2 sidebands.

Rotor level	KCl: NO_2^-			KBr: NO_2^-		
	Ground	ν_2	ν_1	Ground	ν_2	ν_1
2	7.82	8.22	7.0	5.75	5.88	5.5
1^+	2.34	2.31		1.94	1.84	
(1)	(2.17)	(2.15)	2.0	(1.74)	(1.59)	1.2
1^-	2.00	1.99		1.36	1.30	
0	0.00	0.00	0.00	0.00	0.00	0.00

vibrational modes of the cleaved $\text{KBr}:\text{NO}_2^-$ and $\text{KCl}:\text{NO}_2^-$ samples. The much broader ν_1 ($\sim 1320 \text{ cm}^{-1}$) bands, which range 1.3 to 3.5 cm^{-1} in width, mask this splitting, so only the mean energy is shown for the ν_1 symmetric vibrational modes.

5. Stress dependence of ν_2 reorientational tunneling fine structure

Figure 23 demonstrates that uniaxial stress applied along the $[110]$ crystal direction at low temperatures splits the $P(1)$, $R(0)$, and $R(1)$ bands of the $\text{KCl}:\text{NO}_2^- \nu_2$ band. The absorption coefficient is shown for interferometer light polarized along different crystal axes parallel and perpendicular to the stress axis: Figs. 23(a) $\epsilon_{110} \parallel \sigma_{110}$, 23(b) $\epsilon_{1-10} \perp \sigma_{110}$, and 23(c) $\epsilon_{001} \perp \sigma_{110}$. The lines observed at zero stress move and become strongly polarized under $[110]$ stress, no new lines appear. Note that for $\epsilon \perp \sigma_{110}$, the $P(1^- \rightarrow 0)$ and $R(0 \rightarrow 1^-)$ bands move together toward the Q at 802 cm^{-1} , become very narrow, and their peak ratio approaches one. Other lines in the spectrum move away from the Q band and either remain at nearly constant width or rapidly broaden.

Figure 24 presents similar measurements but for stress along the $[100]$. Larger shifts are produced with $[110]$ stress than with $[100]$ stress. For an applied $[110]$ uniaxial

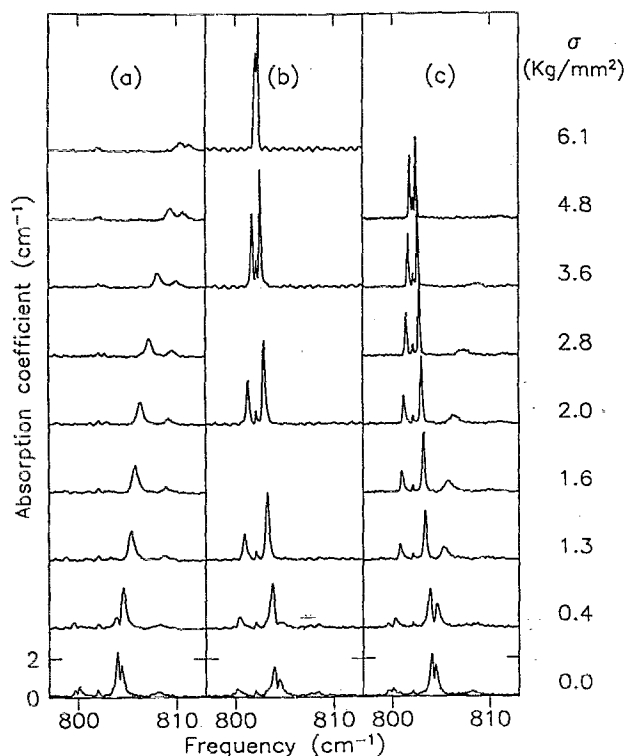


FIG. 23. Uniaxial stress dependence of the $\text{KCl}:\text{NO}_2^- \nu_2$ absorption spectrum under $[110]$ stress at 1.7 K . The IR light is polarized (ϵ) along different crystal axes parallel and perpendicular to the stress axis (σ): (a) $\epsilon_{110} \parallel \sigma_{110}$ (0.06 cm^{-1} resolution), (b) $\epsilon_{1-10} \perp \sigma_{110}$ (0.1 cm^{-1} resolution), and (c) $\epsilon_{001} \perp \sigma_{110}$ (0.06 cm^{-1} resolution).

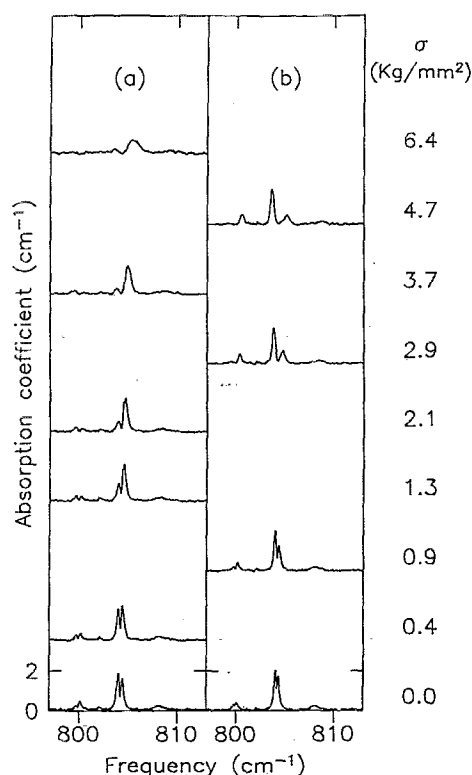


FIG. 24. Uniaxial stress dependence of $\text{KCl}:\text{NO}_2^- \nu_2$ absorption spectrum under $[100]$ stress. The IR light is polarized (ϵ) parallel and perpendicular to the stress axis (σ): (a) $\epsilon_{100} \parallel \sigma_{100}$ and (b) $\epsilon_{001} \perp \sigma_{100}$. No new lines appear in the spectrum. The 804 and 800 cm^{-1} components are polarized less and shift smaller amounts than for applied $[110]$ stress. The 808 cm^{-1} sideband remains unpolarized.

stress greater than $\sim 1 \text{ kg/mm}^2$ (values as large as $\sim 6 \text{ kg/mm}^2$ were used), the absorption bands become completely polarized along $[110]$, $[1-10]$, and $[001]$ crystal directions. Application of large uniaxial stress at 1.7 K for 2 h and subsequent stress removal returns the $\text{KCl}:\text{NO}_2^- \nu_2$ and ν_1 symmetric vibration band shapes with no apparent dichroism when measured in a 2 min interval after stress removal. However, a *partial* dichroism which relaxes on a 15 min time scale at 1.7 K is observed for the sharp $\nu_3(B_1)$ antisymmetric vibrational mode (i.e., the mode without tunneling fine structure) for the symmetric $(15, 16, 16)$ and $(14, 16, 16)$ isotopic molecules. Since the ν_2 band recovers much more quickly than the ν_3 , the complete polarization of the tunneling sidebands under $[110]$ stress is not due to a reorientation of the fixed O-O axes, but instead is due to the symmetry lowering of the tunneling states and the polarization of initially partially unpolarized transition moments.

The $\text{KCl}:\text{NO}_2^- \nu_2$ tunneling sum-band frequencies observed for different polarizations under $[110]$ stress are displayed in Fig. 25. Each line is polarized along the $[110]$, $[1-10]$, or $[001]$ crystal directions as labeled in Fig. 25. The movement of the $R(0 \rightarrow 1^\pm)$ transitions (starting from 804 cm^{-1}) relative to the more slowly shifting Q line (802.1 cm^{-1}) is representative of the relative movement of $K = 0, 1^-$, and 1^+ and the $K' = 0, 1^-$, and 1^+ energies. For $[110]$

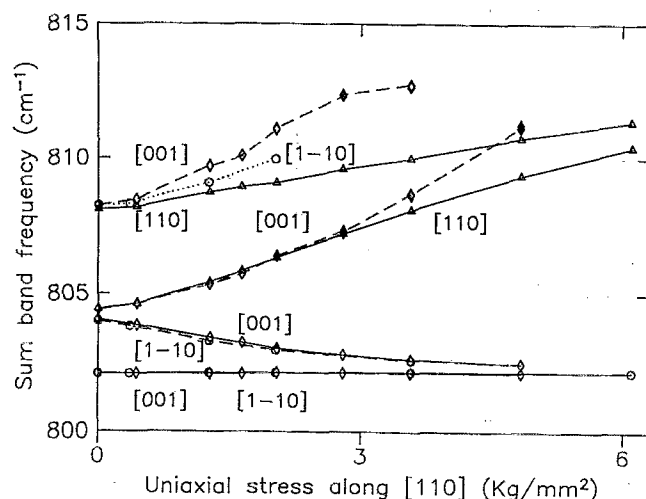


FIG. 25. Absorption line frequency versus $[110]$ uniaxial stress for the $\text{KCl}:\text{NO}_2^-$ ν_2 tunneling sum-band region. At the bottom of the figure, the pure vibrational Q -band frequency shifts very little (0.06 cm^{-1}) from 802.10 cm^{-1} . Compared to the Q , the 804 cm^{-1} $R(0)$ and 808 cm^{-1} $R(1)$ bands shift and split much more rapidly. Each peak is labeled by the polarization in which it is observed. Two groups of peaks can be assigned to two groups of centers that are orientationally inequivalent under $[110]$ stress. The suggested assignment is expressed by the dashed and solid lines connecting the points.

stress above 2 kg/mm^2 , the $K = 1^+$ level lies more than 3 kT above the $K = 0$ level at 1.7 K (1.2 cm^{-1}). Hence, at high stress only the $K = 0$ and 1^- levels are significantly populated and the transitions observed under large $[110]$ stress originate from these two lowest states. The $R(0 \rightarrow 1^-)$ and $P(1^- \rightarrow 0)$ transitions move towards the Q band, narrow, and grow in strength with increased $[110]$ stress. One spectrum (not shown) for $\epsilon_{001} \perp \sigma_{110}$, and $\sigma_{110} = 6\text{ kg/mm}^2$ left the $R(0 \rightarrow 1^-)$ and $P(1^- \rightarrow 0)$ lines unresolved at a spectral resolution of 0.03 cm^{-1} . (This is nearly the homogeneous hole width found in Sec. III B 3.) The ratio of the $R(0 \rightarrow 1^-)$ and $P(1^- \rightarrow 0)$ absorption peak heights follows a Boltzman population factor with an energy splitting of half the difference in transition energies, hence, the separation between the $K' = 0$ to 1^- and $K = 0$ to 1^- levels decrease in the same way with stress. The movement of the $K = 0$ and 1 levels with stress or strain is illustrated on the right of Fig. 21. The level shift curves in Fig. 21 are constructed from fits to $[110]$ stress data from 0 to 3 kg/mm^2 in Fig. 25. The almost complete removal of inhomogeneous broadening in the $P(1^- \rightarrow 0)$ and $R(0 \rightarrow 1^-)$ lines is consistent with the slopes of the $K, K' = 0, 1^-$ energies becoming more nearly the same at large stress. In contrast, the increased width of the inhomogeneously broad $R(0 \rightarrow 1^+)$ $[110]$ and $[001]$ polarized components under $[110]$ stress indicates that these transitions are between energy levels that have different dependences on stress (i.e., the 0 and 1^+ energies move away from each other). Examination of the $R(0 \rightarrow 1^+)$ line shows that it further splits with orthogonal $[1-10]$ and $[001]$ polarizations for large $[110]$ applied stress. Careful examination of the lower-frequency $R(0 \rightarrow 1^-)$ line shows

that there are also different orthogonal transitions for $R(0 \rightarrow 1^-)$.

From uniaxial stress results on the $\nu_3(B_1)$ and $[\nu_2 + \nu_3](B_1)$ modes, which are pure vibrational transitions lacking tunneling fine structure, the O-O axis is found to be oriented along a $\langle 111 \rangle$ crystal axis. This is in agreement with a recent reanalysis of polarized Raman scattering³⁹ and polarized UV luminescence.⁵⁹ Since the O-O axes lie along $\langle 111 \rangle$ crystal directions, there are two inequivalently oriented groups of $\text{KCl}:\text{NO}_2^-$ defects with respect to an applied $[110]$ stress. [These two groups have their O-O axes in the (110) and $(1-10)$ crystal planes.] The two sets of $R(0 \rightarrow 1^\pm)$ lines are interpreted as belonging to the two orientationally inequivalent groups of $\text{KCl}:\text{NO}_2^-$ defects.

The broader, higher-frequency $R(1)$ lines allow two possible interpretations for the $K, K' = 2$ levels. For small $[110]$ stress ($< 2\text{ kg/mm}^2$), three polarized $R(1^\pm)$ lines are observed. These originate near 808 cm^{-1} in Figs. 23 and 25. The $[1-10]$ polarized $R(1)$ line decreases in strength up to 2 kg/mm^2 as the $K = 1^+$ level is thermally depopulated, so the $[1-10]$ polarized $R(1)$ line is an $R(1^+)$ transition. Since the remaining $R(1)$ transitions that are polarized along $[110]$ and $[001]$ crystal directions do not decrease in integrated strength with $[110]$ stress, these must be transitions from the $K = 1^-$ state, which moves closer to the ground state. The $[110]$ polarized $R(1)$ transition narrows slightly and the $[001]$ $R(1)$ transition broadens, indicating that the $K' = 2$ levels for these two differently polarized transitions respectively follow and move away from the $K = 1^-$ level with stress. The simplest interpretation is that the $[001]$ and $[110]$ polarized $R(1^-)$ lines belong to the two inequivalently oriented groups of $\text{KCl}:\text{NO}_2^-$ defects under $[110]$ stress, and that the $K = 2$ and $K' = 2$ levels are singly degenerate. However, the very different movement of the $R(1^- \rightarrow 2)$ transitions could also be interpreted with a double degenerate $K' = 2$ level and different selection rules for the orientationally different groups of centers. A combination of uniaxial stress and temperature dependence would be required to determine the degeneracy of the $K, K' = 2$ levels. Because of the present $K, K' = 2$ level degeneracy ambiguity, we represent the $K, K' = 2$ levels in Fig. 21 with a single level and do not show movement of this level with stress.⁶⁰

IV. DISCUSSION

A. $\text{KI}:\text{NO}_2^-$ hole burning

The vibrational modes of $\text{KI}:\text{NO}_2^-$ exhibit the remarkable property at low temperatures that most of the PIRSH's show a few tens or hundreds of MHz hole width, but that the ν_1 band appears to be uniformly burned with a much wider width of 90 GHz . This finding is consistent with an earlier hypothesis that the ν_1 mode is lifetime broadened by rapid phonon decay to the ν_3 mode, while the homogeneous width of the ν_2 band is phonon modulation broadened.^{15,30} The very asymmetric absorption shape for this homogeneous mode probably results from resonance effects similar to those found for absorbates on surfaces⁶¹ or autoionizing electronic states of atoms,⁶² in which a discrete state is in

resonance with a continuum of states. When the symmetry of the defect is lowered by replacement of (14, 16, 16) with (14, 16, 18), the 9 cm^{-1} doublet observed in Raman scattering also appears in absorption (see Table II). Our result is also consistent with the interpretation that the ν_1 mode in $\text{KI}:\text{NO}_2^-$ consists of a Fermi resonance doublet between the ν_1 mode and $[\nu_3 + \text{in-band phonon mode}]$ sideband when observed in Raman scattering.^{18,37} In this interpretation, the resonance strongly couples the ν_1 and ν_3 modes via a local phonon which results in rapid decay of the ν_1 resonance into ν_3 . Despite the body of evidence that the ν_1 mode shapes are due to resonance effects, there is disagreement in the assignment of symmetries to the modes in these resonances.³⁹ In any case, the $\text{KI}:\text{NO}_2^-$ ν_1 resonance width appears to be lifetime limited with a lifetime on the order of 11 ps at 1.6 K.

The PIRSH erasure times can be compared with the relaxation times obtained from dielectric function measurements⁵³ and UV stress-induced linear dichroism (SILD) relaxation studies.^{17,19} The temperature dependence of the dielectric function at $\sim\text{kHz}$ frequencies shows that the permanent dipole moment is frozen into the lattice below 8 K. However, an anomalous dispersion is observed above 8 K that is associated with reorientation of the defect with an activation energy of 117 cm^{-1} . The temperature at which the $\text{KI}:\text{NO}_2^-$ defect dipole begins to reorientationally respond to an applied field of $\sim\text{kHz}$ frequencies is also the temperature above which detectable holes are not burned. This is consistent with our earlier report that $\text{KI}:\text{NO}_2^-$ persistent infrared hole burning involves reorientation of the NO_2^- molecule at the lattice site.⁴⁴

The PIRSH relaxation times correspond to those obtained from SILD relaxation of the UV modes. SILD relaxation was measured over the temperature interval from 5 to 6.5 K, and the relaxation time was found to vary from 1 to several hundred seconds.^{17,19} This is also the temperature range for which the long burn time infrared hole depth is found to decrease. The UV SILD relaxation time is found to obey an Arrhenius relationship $\tau = \tau_0 e^{\Delta E/kT}$ with $\tau_0 = 3 \times 10^{-9}\text{ sec}$ and $\Delta E = 90\text{ cm}^{-1}$. If this relation were to hold down to 1.5 K, then the SILD relaxation time would be many orders of magnitude longer than the PIRSH relaxation time of 3000 sec at 1.5 K. However, the long burn time hole depth does not vary between 1.5 and 5 K, which suggests that reorientational relaxation time for unannealed $\text{KI}:\text{NO}_2^-$ has a temperature-independent value below 5 K (and presumably the SILD relaxation time is constant, as well). This temperature independence indicates that the molecules undergo weak tunneling transitions accompanied by phonon emission between orientations made inequivalent by crystal strains between 1.5 and 5 K. Above 5 K, thermally activated reorientation over barriers to rotation must dominate over the tunneling transitions.

The PIRSH depth dependence on intensity and temperature suggests that the depth is determined by a competition between the hole production and decay rates. If the hole burning intensity is lowered, a lower limit is reached below which no detectable hole is produced. If the temperature is raised, the hole relaxation rate increases and the long-time equilibrium hole depth becomes smaller until at the hole

erasure temperature of 8 K, no detectable hole is produced. To quantify these dependences a model of this intensity dependent hole depth is now presented which is based on a competition between hole production and decay rates.

B. Intensity dependence of the PIRSH depth

A qualitative picture for the key ingredients with which to characterize the intensity dependence of the PIRSH depth can be gained by first reviewing *transient* hole burning. When the laser field becomes intense enough so that the stimulated transition rate is comparable to or larger than the spontaneous decay rate, then the excited state population approaches the ground-state population. Here, very large intensities are usually needed because the spontaneous decay time T_1 may be short (see, for example, Refs. 63 and 64). For homogeneously broadened lines, the intensity⁶⁵ where the stimulated and spontaneous decay rates are comparable is the transient incoherent saturation intensity $I_s = (h\nu)/(\sigma T_1)$. Analogously, *persistent* hole formation involves a competition between the hole production process and spontaneous relaxation between the ground states.⁶⁶ The underlying differences are twofold: persistent hole production does not involve intensity-dependent stimulated transitions into the hole burned ground state and the lifetime of a persistent hole is much greater than the excited state lifetime.

Next, it will be shown that there is still some persistent hole burning intensity I_h below which the hole size decreases to immeasurable values regardless of the burn time. Crudely speaking, I_h can be written by reducing the peak cross section by the quantum efficiency to give $I_h = (h\nu)/(\eta\sigma\tau)$. (To be placed on firmer footing shortly.) In the infrared, typical values for centers that have been hole burned are $h\nu \sim 10^{-20}\text{ J}$, $\eta \sim 10^{-5}$, $\sigma \sim 10^{-15}\text{ cm}^2$, and $\tau \sim 1\text{ h}$. Here, $I_h \sim 30\text{ mW/cm}^2$. This intensity is just within the range $< 100\text{ mW/cm}^2$ available at a sample from a single mode of an Pb salt diode laser. Hence, it is important to quantify how the ground-state relaxation processes affect the hole burning depth at low intensities.

In a persistent hole burning experiment, the laser intensity and spectral density of absorbing defects are functions of position and time. A collimated laser beam restricts the spatial variation in I and n to $I = I(x, t)$ and $n = n(x, \nu_c, t)$. The geometry is identified in Fig. 26(a). All intensities are internal intensities, i.e., reflections at interfaces are neglected. The internal intensity at $x = 0$ is I_0 . The intensity $I(x, t)$ varies with position x from the front surface because of the absorption centers, and with time t because the absorption centers with frequency near ν_L are being hole burned. The laser beam at frequency ν_L is assumed to have a spectral width much smaller than the homogeneous width of the molecular transition.

Figure 26(b) shows the defect density distribution in the equilibrium ground and nonequilibrium intermediate states, and the hole burning and relaxation pathways. The absorption centers have unburned ground and hole burned intermediate states with associated transition frequencies of ν_c for the unburned ground state and ν for the antihole intermediate state. The laser excites unburned absorption centers

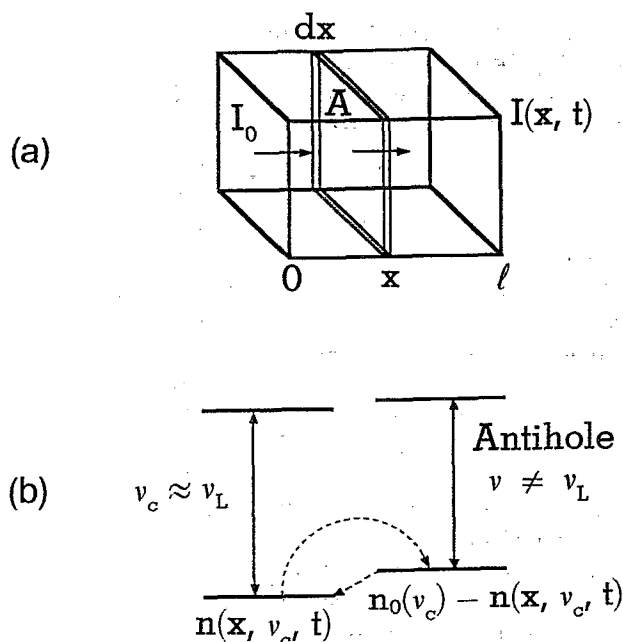


FIG. 26. Hole burning rate equation model with intermediate state relaxation. (a) Picture of the optically thick sample volume of thickness l illuminated with a collimated low-intensity laser of area A at frequency ν_L . (b) Energy-level diagram showing excited state (solid arrows) and ground-state (dashed arrows) transitions. The optical excitation pathway responsible for hole burning is abstracted by the dashed arc between ground states.

with $\nu_c \approx \nu_L$ which occasionally follow a hole burning pathway abstracted by a dashed arc into antihole or hole burned intermediate states. The hole burning pathway could involve a variety of optical pumping pathways through excited states.^{58,67-69} The only necessary condition is that a hole burning pathway exists, so it is represented by a single dashed arc. Absorption centers in the antihole intermediate states relax and refill the unburned ground states. The initially spatially uniform spectral density of absorbers $n_0(\nu_c)$ (units of per unit volume per unit center frequency interval) is nonuniformly modified by the spatially varying intensity $I(x, t)$ resulting in a spectral density of absorbers $n(x, \nu_c, t)$ in the unburned ground state and $n_0(\nu_c) - n(x, \nu_c, t)$ in the relaxing antihole states.

Holes and homogeneous line widths at low intensity are often Lorentzian shaped, so for this discussion we define the spectral cross section as

$$\sigma(\nu) = \frac{\sigma_0(\gamma/2)^2}{\nu^2 + (\gamma/2)^2}, \quad (1)$$

where γ is the full width at half maximum, and σ_0 is the peak cross section (in cm²). A defect with center frequency ν_c has cross section $\sigma(\nu - \nu_c)$.

The total time rate of change of the spectral density of defects at x and ν_c is the sum of the rates of burning and relaxation of the defect spectral density: $dn/dt = R_{\text{relax}} - R_{\text{burn}}$. The rate of defect spectral density burning is the rate of photon absorption times the probability per absorbed photon per defect that a defect is hole burned (η). Laser photons arrive at slab x in Fig. 26(a) at the rate

$P(x)/h\nu_L$, where $P(x)$ is the power in the laser beam. The fraction of laser photons arriving at x that are absorbed in dx (per unit center frequency interval) by defects with center frequency ν_c is $\sigma(\nu_L - \nu_c)n(x, \nu_c, t)dx$. Then, the rate of defect spectral density burning is the rate of photon absorption per unit center frequency interval per unit volume ($A dx$) times the quantum efficiency. Hence,

$$R_{\text{burn}} = \sigma n \frac{I}{h\nu_L} \eta. \quad (2)$$

Since a hole burned ground state is assumed to have a transition frequency far from the laser frequency (the antiholes do not absorb at the laser frequency), no accounting of the antihole transition frequency is necessary. The relaxation rate of the hole burned defect spectral density is

$$R_{\text{relax}} = [n_0(\nu_c) - n(x, \nu_c, t)]/\tau, \quad (3)$$

when all of the defects are assumed to have the same decay time τ . Hence, for an intensity smaller than the transient saturation value, the total time rate of change of the spectral density for defects at center frequency ν_c is

$$\frac{dn(x, \nu_c, t)}{dt} = \frac{n_0(\nu_c) - n(x, \nu_c, t)}{\tau} - \sigma(\nu_L - \nu_c)n(x, \nu_c, t) \frac{I(x, t)}{h\nu_L} \eta. \quad (4)$$

The intensity in Eq. (4) varies in the following way. Only unburned defects are assumed to absorb at the laser frequency. Then, as the radiation traverses dx , absorbers at ν_c produce a change in the intensity of $-I\sigma(\nu_L - \nu_c)n(x, \nu_c, t)d\nu_c dx$. Adding up the changes due to defects with different center frequencies ν_c gives

$$\frac{dI}{dx} = -I \int_{-\infty}^{+\infty} \sigma(\nu_L - \nu_c)n(x, \nu_c, t)d\nu_c. \quad (5)$$

Equations (4) and (5) are coupled equations from which the long burn time intensity $I(x, t \rightarrow \infty) = I(x)$ can be obtained. For $t \rightarrow \infty$, $dn/dt = 0$ and Eq. (4) becomes

$$n(x, \nu_c, t \rightarrow \infty) = \frac{n_0(\nu_c)}{1 + [I(x, t \rightarrow \infty)/h\nu_L]\sigma(\nu_L - \nu_c)\eta\tau}. \quad (6)$$

Substituting $n(x, \nu_c, t \rightarrow \infty)$ into Eq. (5) eliminates $n(x, \nu_c, t \rightarrow \infty)$ giving

$$\frac{dI(x)}{dx} = -I(x) \times \int_{-\infty}^{+\infty} \frac{n_0(\nu_c)\sigma(\nu_L - \nu_c)}{1 + [I(x)/h\nu_L]\sigma(\nu_L - \nu_c)\eta\tau} d\nu_c. \quad (7)$$

As expected, an equation with the same form as Eq. (7) is found in transient saturation studies.⁶⁵

Equation (7) is readily solved for two limits where $n_0(\nu_0)$ is either homogeneous or very inhomogeneous. The homogeneous case corresponds to a persistent bleaching of an entire mode as shown for the ν_1 band in Fig. 14 and it will be treated first.

For a homogeneously broad mode, all the transitions have the same center frequency ν_0 , $n_0(\nu_c) = n_0\delta(\nu_0 - \nu_c)$, and Eq. (7) integrates to

$$\alpha_0 x = -\ln \frac{I(x)}{I_0} + \frac{1}{I_h} [I_0 - I(x)], \quad (8)$$

where

$$\alpha_0 = n_0 \sigma(\nu_L - \nu_0) \quad \text{and} \quad I_h = \frac{h\nu_L}{\sigma(\nu_L - \nu_c)\eta\tau}. \quad (9)$$

The hole burning intensity I_h at the peak of the homogeneous mode shall be denoted by a superscript p so

$$I_h^p = \frac{h\nu_L}{\sigma_0\eta\tau}. \quad (10)$$

In a persistent hole burning experiment, the hole depth is measured as the fractional change in the absorption coefficient, $(\Delta\alpha)/\alpha$, obtained from the measured intensities and corresponding sample transmittance. Since the (internal) burned transmittance $T_{\text{burn}} = T_b = I(l)/I_0 = e^{-\alpha_b l}$, where l is the sample thickness, we can rewrite Eq. (8) as an implicit expression for the long burn time absorption coefficient α_b in terms of the incident (internal) intensity I_0 , the hole burning intensity I_h , and the unburned absorption strength at the laser frequency α_0 giving

$$I_0 = I_h \left(\frac{[\alpha_0(\nu_L) - \alpha_b(\nu_L)]l}{1 - e^{-\alpha_b(\nu_L)l}} \right). \quad (11)$$

For the very inhomogeneously broadened case, the spectral density of absorbers $n_0(\nu_c) = n_0$ (units of $\text{cm}^{-3} \text{Hz}^{-1}$) is flat within a few homogeneous widths about the laser frequency hence it can be taken outside of integral in Eq. (7). Solving it gives

$$\frac{dI}{dx} = -\pi n_0 \frac{\gamma}{2} \sigma_0 I \left(1 + \frac{\sigma_0 \eta \tau}{h\nu_L} I \right)^{-1/2}. \quad (12)$$

Since, in this inhomogeneous case,

$$\alpha_0 = \int n_0 \sigma(\nu_L - \nu_c) d\nu_c = \pi n_0 (\gamma/2) \sigma_0, \quad (13)$$

the equation for the spatial variation of the intensity when a persistent hole is burned into an inhomogeneous band, becomes

$$\frac{dI}{dx} = -\alpha_0 I \left(1 + \frac{I}{I_h^p} \right)^{-1/2}. \quad (14)$$

Integrating from 0 to x and I_0 to $I(x)$ gives an implicit expression for $I(x)$ in terms of I_0 , I_h^p , and α_0 , namely,

$$\begin{aligned} \alpha_0 x &= 2 \left[(1 + I_0/I_h^p)^{1/2} - (1 + I/I_h^p)^{1/2} \right] \\ &+ \ln \left(\frac{[(1 + I_0/I_h^p)^{1/2} - 1]}{[(1 + I_0/I_h^p)^{1/2} + 1]} \right) \\ &\times \frac{[(1 + I/I_h^p)^{1/2} + 1]}{[(1 + I/I_h^p)^{1/2} - 1]}. \end{aligned} \quad (15)$$

For intensities small compared to I_h^p , Eq. (15) found here for the inhomogeneous case reduces to the homogeneous expression, Eq. (8) with $\nu_L = \nu_0$. In other words, at very small intensities the hole depth behaves as if only defects with center frequencies identical to laser frequency are involved, since the relaxation rate of defects away from the laser frequency overwhelms the smaller hole burning rate.

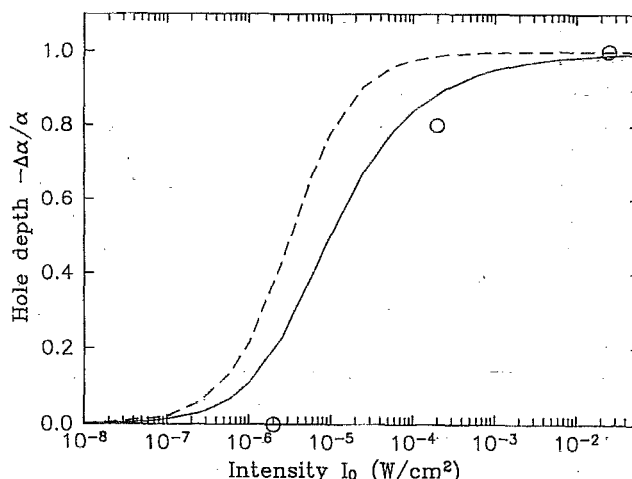


FIG. 27. Comparison of the $\text{KI}:\text{NO}_2^-$ asymptotic hole depth intensity dependence for the bending mode of $\text{KI}:\text{NO}_2^-$ with a rate equation model. The open circles are data for $\text{KI}:\text{NO}_2^-$ at 1.5 K. The model has no free parameters.

C. Hole-depth calculation versus experimental results for $\text{KI}:\text{NO}_2^-$

Figure 27 shows three experimental values for the $\text{KI}:\text{NO}_2^-$ ν_2 mode hole-depth dependence $\Delta\alpha/\alpha_0$ on intensity. These values are compared with the predictions of the homogeneous [Eq. (8)] and inhomogeneous [Eq. (15)] linewidth models. Since all of the parameters that go into the hole burning intensity I_h^p , namely $h\nu$, σ , η , and τ , are independently known, this comparison provides a test of a rate equation model. In Fig. 27, the dashed curve is the “hole” depth (fractional change in peak absorption coefficient) for a homogeneous mode, and the solid curve is for an inhomogeneous mode.

In detail, the analysis shown in Eq. (27) proceeds as follows. First, the experimental hole depths shown in Fig. 27 were recorded at three intensities for $l = 0.079$ cm and $\alpha_0 l = 1.0$ at 1.5 K. The hole burning intensity that is used in this comparison for the $\text{KI}:\text{NO}_2^-$ ν_2 mode is $I_h^p = h\nu/(\eta\sigma_0\tau) = 2.5 \times 10^{-6} \text{ W/cm}^2$, which is computed from the experimentally determined values $h\nu = 1.6 \times 10^{-20} \text{ J}$, $\sigma_0 = 2.1 \times 10^{-16} \text{ cm}^2$, $\eta = 10^{-2}$, and $\tau = 3000 \text{ sec}$ (at 1.6 K). Using these values for $\alpha_0 x = \alpha_0 l$ and I_h^p in Eqs. (8) and (15), the transmitted intensity I and the final burned absorption coefficient $\alpha_b = -\ln(I/I_0)/l$ are computed numerically for various input intensities I_0 . Finally, the hole depth $\Delta\alpha/\alpha_0 = (\alpha_b - \alpha_0)/\alpha_0$ is computed and displayed versus I_0 in Fig. 27.

The rate equation model for an inhomogeneous mode (solid curve in Fig. 27) is within a factor of 3–5 of the measured hole depth versus intensity for the $\text{KI}:\text{NO}_2^-$ ν_2 mode. Since η is computed from nine experimentally determined quantities, it is only good to within an order of magnitude, and I_h^p is also expected to be as uncertain. Hence, within experimental uncertainty a competition between hole formation and relaxation explains the intensity dependence of the hole depth.

Note that for a given laser intensity smaller changes in absorption are produced in an inhomogeneous mode than at the peak of a homogeneous mode. For the inhomogeneously broadened case defects away from the laser frequency have a proportionally smaller rate of hole burning than defects centered at the laser frequency, but have the same rate of hole decay. Hence, nearly resonant defects contribute to the unburned absorption but contribute less to the final hole depth. It is interesting that a hole relaxation time of nearly an hour can compete with the formation of a hole at intensities that are routinely used in lead salt diode laser hole burning spectroscopies. In the following sections, the hole burning results for $\text{KBr}:\text{NO}_2^-$ and $\text{KCl}:\text{NO}_2^-$ are presented and discussed in light of the intensity-dependent hole-depth result found here for $\text{KI}:\text{NO}_2^-$.

D. Comparison of NO_2^- hole burning results in potassium halides

The relative ease of PIRSH burning in $\text{KI}:\text{NO}_2^-$ compared to $\text{KCl}:\text{NO}_2^-$ and $\text{KBr}:\text{NO}_2^-$ can be understood by inspecting the values of the different parameters related to the hole production and decay rates listed in Table IV. For $\text{KI}:\text{NO}_2^-$, it was found that the hole depth is determined by a competition between hole production and decay rates. The probability that a defect will be hole burned is proportional to its peak cross section σ for absorbing a photon and proportional to the quantum efficiency η for changing ground states after absorbing a photon. The larger these quantities, the greater the rate of hole production for a given intensity. The hole formation time is a fraction of a minute in $\text{KI}:\text{NO}_2^-$ compared to many minutes for KCl and KBr at the highest diode laser intensities used ($\sim 25 \text{ mW/cm}^2$). This rate is much larger in $\text{KI}:\text{NO}_2^-$ than in KCl or KBr because of the much larger quantum efficiency (Table IV). In addition, the shorter NO_2^- hole relaxation times for the KCl and KBr hosts make it more difficult to burn a deep hole at a given intensity than in KI. The greater ease of PIRSH burning in $\text{KI}:\text{NO}_2^-$ is expressed by its lower I_h^p (see the last column of Table IV).

It is now possible to understand the negative hole burn-

ing results obtained for some of the homogeneously broadened ν_1 bands. For $\text{KI}:\text{NO}_2^-$, rapid decay of the ν_1 mode into the ν_3 mode by one-phonon decay results in a very broad ν_1 -mode homogeneous width ($\sim 3 \text{ cm}^{-1}$). The very broad NO_2^- ν_1 modes in KCl and KBr ($\sim 1.3\text{--}3.5 \text{ cm}^{-1}$) are similarly within one-phonon energy of the ν_3 mode, and also appear to be homogeneously broad. The larger widths of these modes compared with the ν_2 cases results in a 30- to 100-fold reduction in peak cross section; hence, the main reason why the ν_1 modes (and the broader ν_2 sidebands) are not hole burned is that our diode lasers are not intense enough.

For narrow lines such as the $\text{KCl}:\text{NO}_2^-$ ν_3 (B_1) mode, special polarization properties provide the most likely explanation for the lack of hole burning. Because of the $\langle 111 \rangle$ orientated transition-dipole moments,^{39,59} the narrow $\text{KCl}:\text{NO}_2^-$ [$\nu_2 + \nu_3$] (B_1) mode, which has the same symmetry as the ν_3 (B_1) mode, would not hole burn for the laser burn polarization in a $\langle 100 \rangle$ crystal axis. We speculate that this mode is nearly homogeneously broad, and so a reorientation would not produce a change in absorption strength for $\langle 110 \rangle$ laser polarization.

E. Origin of infrared satellite holes in the ν_2 absorption spectrum of $\text{KCl}:\text{NO}_2^-$

Narayanamurti *et al.* proposed that NO_2^- ions in KCl and KBr have reorientational tunneling states at low temperatures,²⁶ and a large body of experimental data now supports that idea. Their observation that the infrared tunneling structure does not appear in combination with the ν_3 (B_1) mode, with its transition dipole moment parallel to the O-O axis, is interpreted to indicate that one molecular axis parallel to the O-O axis is fixed in the lattice, and that NO_2^- exhibits one-dimensional tunneling motion connected with rotation about this axis. Transitions associated with rotational motion have been observed on the vibrational modes in Raman scattering,^{13,21,34-36} ultraviolet absorption,^{7,8,10,11,13,20-23} and ultraviolet emission studies.^{7-9,13,15,21}

Given that one-dimensional (1D) rotational motion occurs for this C_{2v} molecule in KCl and KBr, the object now is to account for the multiple persistent satellite holes that can

TABLE IV. Hole burning parameters for NO_2^- defects in single crystals at 1.6 K.

Host	$\Delta\nu_{\text{hole}}$ (GHz)				τ (min)	η^a	σ^a (10^{-17} cm^2) (I_h^p) ^b (W/cm^2)	
	ν_2	ν_3	ν_1	$(\nu_2 + \nu_3)$				
KCl	0.75 ^c	0.3 ^d	e	e	15	$\sim 10^{-4}$	4	1.8×10^{-2}
KBr	1.0 ^c (0.35) ^d	0.3 ^d	e		0.5	$\sim 10^{-4}$	8	2.6×10^{-1}
KI	0.037 ^d	0.060 ^d	$\sim 90^f$	0.5	50	$\sim 10^{-2}$	21	2.5×10^{-6}

^a Measured on the ν_2 -R(0) mode for KCl and KBr.

^b The persistent hole burning intensity is calculated from $I_h^p = h\nu/(\eta\sigma\tau)$ for the ν_2 mode.

^c Tunneling sideband PIRSH width in the ν_2 -R(0) mode.

^d Pure vibrational transition (or Q) PIRSH width.

^e No detectable change is produced with $\sim 25 \text{ mW/cm}^2$.

^f The entire oddly shaped ν_1 mode changes strength for the (14,16,16) isotope.

be generated in the ν_2 absorption band. It is shown here that strain-induced degenerate level splitting dominates over level shifts and it is this single level splitting which produces the characteristic V-shaped notches.

In general, strain-induced changes in energy levels can be expressed as algebraic combinations of components of the strain tensor at the defect site. A singly degenerate level shifts with strain, and a doubly degenerate level both shifts and splits.⁷⁰ As for the one-dimensional rotor diagram shown in Fig. 21, the energy shift of the $K = 0$ level at E_0 is denoted by S_0 and the shift and splitting of the $K = 1$ level at E_1 is denoted by $S_1 \pm \Delta_1$ (and similarly for the K' levels). The four transition energies in which satellite holes have been observed are

$$\begin{aligned} R(0 \rightarrow 1^+) &= (E'_1 - E_0) + (S'_1 - S_0) + \Delta'_1, \\ R(0 \rightarrow 1^-) &= (E'_1 - E_0) + (S'_1 - S_0) - \Delta'_1, \\ P(1^+ \rightarrow 0) &= (E'_0 - E_1) + (S'_0 - S_1) - \Delta_1, \\ P(1^- \rightarrow 0) &= (E'_0 - E_1) + (S'_0 - S_1) + \Delta_1, \end{aligned} \quad (16)$$

in accord with the notation used in Fig. 21. When hole burning occurs in the transition $R(0 \rightarrow 1^+)$, for instance, the laser frequency selects the value of $(S'_1 - S_0) + \Delta'_1$. Selecting this value does not necessarily fix the individual values of S'_1 , S'_0 , S_0 , S_1 , Δ_1 , and Δ'_1 since the quantities S and Δ are in general different algebraic combinations of many strain tensor components.⁷⁰ Due to this multidimensional inhomogeneous broadening, selecting defects with a given transition frequency is not necessarily the same as selecting identical defect sites. Although satellite holes with the same hole width as the hole at the laser burn frequency need not be observed, such identical satellite holes are observed for $\text{KCl}:\text{NO}_2^-$ as illustrated in Figs. 16 and 17.

Further examination of Fig. 17 shows that the $R(0)$ doublet laser burn frequency and satellite holes are shifted the same absolute amounts to either side of the notch at 804.25 cm^{-1} . This symmetric splitting indicates that the difference in level shifts $(S'_1 - S_0)$ is negligible compared to the splitting Δ'_1 of the $K' = 1$ level within the inhomogeneous $R(0)$ doublet. Laser selection of a particular $R(0)$ transition frequency is then the same as selecting a particular Δ'_1 splitting value for the $K' = 1$ degenerate reorientational tunneling levels of $\text{KCl}:\text{NO}_2^-$. This dominance of the splittings over the difference in level shifts is also why the $R(0)$ and $P(1)$ notch positions at 804.25 and 799.93 cm^{-1} shown in Fig. 10 remain fixed in plastically deformed samples. The equal spacing of satellite holes in the $R(0)$ and $P(1)$ bands of Fig. 16 shows that not only does the hole burning laser frequency select a particular Δ'_1 value, but it also selects an identical Δ_1 . In other words, the small, random strain splitting of the tunneling states is identical in the ν_2 ground and excited states.

There have been many refinements and corrections to the tunneling diagrams for $\text{KCl}:\text{NO}_2^-$ and $\text{KBr}:\text{NO}_2^-$. Two basic approaches have been used: (1) assume a symmetry for the reorientation potential energy of the molecule in the lattice, and adjust barrier parameters to fit the observed spectra, or (2) use results from temperature-dependent spectra to construct the level diagram without model assumptions.

In all methods that provide qualitatively correct results, a molecular axis parallel to the O-O axis is fixed in the crystal and the molecule performs one-dimensional tunneling connected with rotation about this axis. Twofold symmetric models have been assumed,^{22,26,48} but these miss the $K = 1$ level degeneracy.⁷ Subsequently, fourfold potential models have been attempted, which preserve the $K = 1$ level degeneracy and provide fair descriptions of lower resolution spectra.^{10,11,21,49} However, our uniaxial stress results, which are in agreement with a reanalysis of polarized Raman³⁹ and UV luminescence data,⁵⁹ indicate that the O-O axis is oriented along $\langle 111 \rangle$ crystal directions. With this O-O axis orientation, there should be a threefold reorientation potential for the molecule. Fits to NO_2^- tunneling spectra using threefold potential models have not yet appeared in the literature. Only one previous diagram deduced from the temperature-dependent UV absorption data is in agreement with our results.^{7,13} Even here, absorption spectroscopy alone does not have the resolving power to reveal that inhomogeneous broadening within the $R(0)$ and $P(1)$ bands is dominated by random strain splitting of the $K = 1$ levels (see the $K = 1$ levels of Fig. 21).

We now summarize the conditions which produce infrared satellite holes in $\text{KCl}:\text{NO}_2^-$. Each $\text{KCl}:\text{NO}_2^-$ defect environment is strained from an average defect configuration of higher symmetry. For $\text{KCl}:\text{NO}_2^-$, the doubly degenerate $K = 1$ level splitting Δ_1 with low strain dominates over the $K = 0$ or 1 level shifts. Hence, laser selection of a vibrational ground-to-excited-state energy-level difference within the $R(0)$ or $P(1)$ bands is the same as selecting a unique splitting value Δ_1 . Laser excitation of the NO_2^- defect causes the $\langle 111 \rangle$ oriented O-O axis to reorient with low probability to one of its three other $\langle 111 \rangle$ orientations. In the new orientation, the crystal strain at the defect site appears different, and the splitting value Δ_1 changes. Since the selected splitting value determines four different energy levels and four different transition energies, removal of absorption strength at the laser frequency also removes absorption strength in three other transitions. These are the satellite holes. If the splitting of a degenerate level Δ_1 at one end of a vibrational transition did not dominate over the shifts S at both ends of the transition, hole burning would not necessarily select identical transition frequencies in other tunneling sideband transitions, and narrow satellite holes would not have been observed.

F. Calculation of the V-shaped band in the ν_2 absorption spectrum of $\text{KCl}:\text{NO}_2^-$

1. Source of the notch

Another characteristic feature which needs to be explained is the origin of the V-shaped notches in the inhomogeneously broadened $P(1)$ and $R(0)$ bands of ν_2 spectrum. The infrared absorption coefficients for the $\text{KCl}:\text{NO}_2^-$ and $\text{KBr}:\text{NO}_2^-$ ν_2 $R(0)$ and $P(1)$ bands are doublets each with a nonzero splitting value $\Delta_1 \neq 0$ (see Figs. 5, 10, 16, and 17). Moreover, the absorption spectrum produced by the distribution of doublets initially grows linearly with frequency shift from the notch location.

To explain the linearly notched absorption shape, a one-dimensional Schrödinger equation for the NO_2^- rotor in KCl is introduced, namely,

$$-A_\varphi \frac{d^2}{d\varphi^2} \Psi(\varphi) + [V_c(\varphi) + V_s(\varphi)] \Psi(\varphi) = E\Psi(\varphi), \quad (17)$$

where all energies are in wave-number (cm^{-1}) units, A_φ is the appropriate NO_2^- rotational constant,⁷¹ V_c is the unstrained crystal potential, and V_s is the additional rotor energy when the crystal site is strained. With $V_s = V_c = 0$, we have a 1D free rotor with energies and wave functions

$$\Psi_K(\varphi) = \frac{e^{iK\varphi}}{\sqrt{2\pi}}, \quad E_K = A_\varphi K^2, \quad K = 0, \pm 1, \pm 2, \dots \quad (18)$$

The $K = 0$ level is singly degenerate, and all other levels are doubly degenerate. The crystal potential for the NO_2^- rotor with the O-O axis fixed in the $\langle 111 \rangle$ direction has threefold rotation symmetry and, in general, contains terms of $3n$ -fold symmetry where n is 1, 2, 3, In first order, the crystal potential does not split or change the relative spacing of the $|K| = 0, 1$, and 2 levels from the free rotor case. (The lowest level split in first order is the $|K| = 3$ level by the sixfold crystal potential term.) However, a twofold strain coupling $V_s(\varphi)$ does split the $|K| = 1$ level in first order. Since our purpose is to qualitatively explain the presence of the notch in the inhomogeneous splitting distribution of the $R(0)$ and $P(1)$ transitions, we will include the strain coupling $V_s(\varphi)$ but ignore the crystal potential $V_c(\varphi)$. It will be seen that this approximation adequately describes the inhomogeneous absorption spectrum of these transitions.

The strain coupling can be written as

$$V_s(\varphi) = \sum_{ij} \epsilon_{ij} [\lambda_1 (n_i n_j - \frac{1}{3} \delta_{ij}) + \lambda_2 (m_i m_j - \frac{1}{3} \delta_{ij})], \quad (19)$$

where the quantity in square brackets is the elastic dipole moment of the NO_2^- defect, $m = (0, 0, 1)$ is the fixed O-O axis orientation, $n = [\cos(\varphi), \sin(\varphi), 0]$ is the orientation of the plane of the molecule, and λ_1 and λ_2 are the strain interaction energies (the coordinates are chosen with the O-O axis along the z axis, and φ is measured from the x axis). A general strain ϵ_{ij} can be written as

$$\epsilon = \begin{pmatrix} A+B & C & F \\ C & A-B & E \\ F & E & A+D \end{pmatrix}. \quad (20)$$

Computing the sum gives the crystal strain perturbation energy

$$V_s(\varphi) = \lambda_1 [B \cos(2\varphi) + C \sin(2\varphi)] + \frac{D}{3} (2\lambda_2 - \lambda_1). \quad (21)$$

The strain perturbation only depends on three components B , C , and D . The D stretch along the O-O axis shifts all energies uniformly to first order, but does not split the degenerate levels. The twofold shear strain in the rotor plane described by two components B and C does not shift the levels, but does split the $|K| = 1$ level. An absorption spec-

trum is a spectrum of energy differences, so an overall shift due to the D term does not appear in the final spectrum; we ignore the D term by subtracting its effect from the energies. The degenerate perturbation theory matrix for the $|K| = 1$ level (with D removed) is

$$\langle \Psi_{\pm 1} | V_s(\varphi) | \Psi_{\pm 1} \rangle = \frac{\lambda_1}{2} \begin{pmatrix} 0 & B - iC \\ B + iC & 0 \end{pmatrix}, \quad (22)$$

which has energy eigenvalues of

$$\Delta_{\pm 1} = \pm \frac{1}{2} \lambda_1 (B^2 + C^2)^{1/2}. \quad (23)$$

A given energy splitting of the $|K| = 1$ level,

$$E_s = 2|\Delta_{\pm 1}| = \lambda_1 (B^2 + C^2)^{1/2}, \quad (24)$$

results from a quadrature sum of two B and C crystal strain components that does not depend on their sign. The energy splitting surface as a function of the rotor plane shear components B and C is a cone. The probability $P(E_s)$ that a randomly selected defect has a splitting E_s is the integral of the product of the probabilities for strain component values along the circumference of the cone at E_s . This circumference is $2\pi(B^2 + C^2)^{1/2} = 2\pi E_s / \lambda_1$, which grows linearly with splitting E_s . In other words, for a smooth distribution of strains the number of possible pairs of strain component values that give a splitting E_s grows linearly with the splitting, and there are no defect centers with both B and C identically zero. The result is a linear V-shaped notch in the inhomogeneous splitting distribution of the $P(1)$ and $R(0)$ transitions.

We now illustrate the inhomogeneous $R(0)$ absorption line shape that results from the restrictive nonlinear splitting dependence on the two strain components given in Eq. (24). The absorption coefficient is computed from

$$\alpha_{R(0)}(\nu) = \int_0^\infty n(E_s) \sigma(\nu, E_s) dE_s, \quad (25)$$

where $n(E_s)$ [units of $1/(\text{cm}^3)(\text{cm}^{-1})$] is the density of centers with splitting E_s ,

$$\sigma(\nu, E_s) = \sigma_{+1,0}(\nu, E_s) + \sigma_{-1,0}(\nu, E_s) \quad (26)$$

is the sum of the absorption cross sections for transitions from $K = 0$ to $K = \pm 1$, and all energies are in cm^{-1} units. The density of centers is

$$n(E_s) = NP(E_s), \quad (27)$$

where N is the equilibrium density of centers in the $K = 0$ state. In a crystal, it is usual to take the distributions of independent strain components to have normal or Gaussian distributions. To compute the spectrum of splittings $P(E_s)$, we assume Gaussian strain distributions centered at zero strain with a standard deviation of strain values given by w . Then,

$$P(E_s) = \int_{-\infty}^{\infty} (dB/w\sqrt{2\pi}) e^{-(1/2)(B/w)^2} \times \int_{-\infty}^{\infty} (dC/w\sqrt{2\pi}) e^{-(1/2)(C/w)^2} \times \delta[E_s - \lambda_1 (B^2 + C^2)^{1/2}] \quad (28)$$

$$= \frac{1}{2} [E_s / (w\lambda_1)]^2 e^{-\frac{1}{2}(E_s/w\lambda_1)^2}. \quad (29)$$

Even though the strain distributions are smooth and non-

zero at zero strain, the spectrum of splittings $P(E_s)$ is zero at zero splitting, rises linearly with slope $1/2(w\lambda_1)^2$, and peaks at $E_s = w\lambda_1$. The distribution $P(E_s)$ is parametrized by the product $w\lambda_1$. Introducing dislocations into the crystal (see Fig. 10) broadens the distribution of strains (increases w) and moves the peaks in absorption outward while maintaining a linear rise in absorption near the notch, but with lower slope. The uniaxial stress data can be used to determine λ_1 so, in principle, the relationship between macroscopic plastic deformation and the corresponding distribution of microscopic strains can be probed.

2. Source of the asymmetric absorption peak heights

The asymmetry in the peak heights arises from variations in the absorption cross section for the two separate transitions with strain. The absorption cross section is⁷²

$$\sigma_{\pm 1,0}(\nu, E_s) = \left(\frac{L^2}{n}\right) \frac{4\pi^2}{\hbar c} \nu_{\pm 1,0} |\mu_{\pm 1,0}|_{\text{av}}^2 f_{\pm 1,0}(\nu), \quad (30)$$

where n is the index of refraction, $L = (n^2 + 2)/3$ is a local field correction,

$$\nu_{\pm 1,0} = \nu_u \pm \frac{E_s}{2}, \quad (31)$$

where $\nu_u = \nu_2 + A_\varphi$ is the unstrained $R(0)$ notch frequency, and

$$f_{\pm 1,0}(\nu) = (1/\pi) [(\gamma/2)/(\nu_{\pm 1,0} - \nu)^2 + (\gamma/2)^2] \quad (32)$$

is the normalized homogeneous absorption line-shape function for a defect with splitting E_s ,

$$|\mu_{\pm 1,0}|_{\text{av}}^2 = \left| \left\langle \pm 1 \left| \frac{E}{E_0} \cdot \mu \right| 0 \right\rangle \right|_{\text{av}}^2, \quad (33)$$

E is the applied electric field with amplitude E_0 , and μ_0 is the ν_2 vibrational transition dipole moment. The subscript av indicates that an average over defect orientations is to be taken. The asymmetry in the transition strengths arises due to the differences in the $|\mu_{\pm 1,0}|^2$ with strain. Expanding the dot product, we have

$$|\mu_{\pm 1,0}|^2 = |\mu_0|^2 \cdot \left| \frac{E_x}{E_0} \langle \pm 1 | \cos(\varphi) | 0 \rangle + \frac{E_y}{E_0} \langle \pm 1 | \sin(\varphi) | 0 \rangle \right|_{\text{av}}^2. \quad (34)$$

Approximate states $|K\rangle$ which depend on φ and the level splitting energy E_s with strain are needed in the approximation we are using that the crystal potential is zero ($V_c = 0$). Rewriting the strain potential Eq. (21) (with D removed) as

$$V_s(\varphi) = E_s \cos(2\varphi + \varphi_0), \quad (35)$$

places the Schrödinger equation [Eq. (17)] in the form of Mathieu's equation⁷³ for which approximate solutions are known for $E_s/A_\varphi \ll 2$. In this basis, $|K = \pm 1\rangle \rightarrow \{\cos(\varphi) \text{ or } \sin(\varphi)\}/(\pi)^{1/2}$ for zero strain, which are linear combinations of the degenerate $K = \pm 1$ solutions in Eq. (18). Computing the matrix elements numerically shows that the strained defect transitions are separately polarized along x

and y [$\langle -1 | \cos(\varphi) | 0 \rangle = \langle +1 | \sin(\varphi) | 0 \rangle = 0$]. The non-zero matrix elements are $|\langle -1 | \sin(\varphi) | 0 \rangle|^2 = |\langle +1 | \cos(\varphi) | 0 \rangle|^2 = \frac{1}{2}$ at zero splitting. The higher-energy $K = 0$ to $+1$ transition decreases approximately linearly in strength and the lower energy $K = 0$ to -1 transition increases approximately linearly in strength with the level splitting. Averaging over the four $\langle 111 \rangle$ O-O axes orientations and over the distribution of shear strain orientations in the rotor plane gives

$$|\mu_{\pm 1,0}|_{\text{av}}^2 = \frac{1}{2} |\mu_0|^2 \left\{ \frac{|\langle +1 | \cos(\varphi) | 0 \rangle|^2}{|\langle -1 | \sin(\varphi) | 0 \rangle|^2} \right\}. \quad (36)$$

The absorption spectrum is now computed by inserting Eqs. (36), (30), and (29) into Eq. (25). Only two parameters are needed to describe the spectrum: the vibrational transition dipole moment $|\mu_0|$ and the peak strain splitting value $w\lambda_1$. The $R(0)$ absorption spectrum is numerically computed with Eq. (25) by reflecting the $K = 0$ to -1 term in the integral about the origin, which places the integral in the form of a convolution involving a single Lorentzian. The full width of the homogeneous Lorentzian line shape used in the calculation is half the hole width for the $\text{KCl:NO}_2^- \nu_2 - R(0)$ transition ($\gamma = 0.013 \text{ cm}^{-1}$).

Figure 28 compares the calculated $\text{KCl:NO}_2^- \nu_2 - R(0)$ line shape with the measured line shape for three levels of crystal strain. In Fig. 28(a) the measured 1.6 K

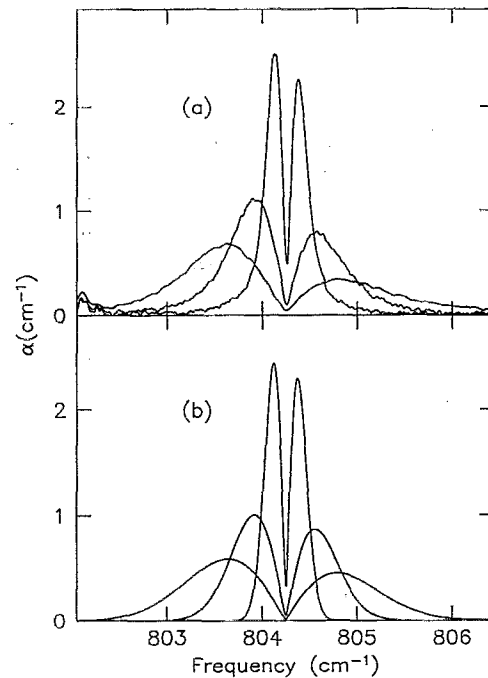


FIG. 28. Comparison of calculated and measured absorption coefficient spectra for the $\text{KCl:NO}_2^- \nu_2 R(0)$ vibrational-tunneling doublet. (a) The measured absorption spectra are shown at 1.6 K for three levels of crystal strain. These samples are freshly cleaved, slightly deformed ($-\Delta l/l < 0.1\%$) with 30 GPa uniaxial pressure at 100 °C, and plastically deformed to $-\Delta l/l = 1\%$ with 56 GPa at 100 °C. (b) Calculated results for inhomogeneously broadened absorption band shapes consisting of degenerate transitions splitting due to a Gaussian distribution of random crystal strains.

absorption spectra are shown for $\text{KCl}:\text{NO}_2^-$ samples that are freshly cleaved, slightly pressed ($-\Delta l/l < 0.1\%$) at 100°C with 30 GPa, and plastically deformed to 1% with 56 GPa. In Fig. 28(b), the calculated spectra are shown for a fixed vibrational-transition-dipole moment of $\mu_0 = 1.7 \times 10^{-19}$ esu cm = 0.17 D and $\omega\lambda_1 = 0.25, 0.64$, and 1.2 cm^{-1} . The calculated absorption spectra for an inhomogeneous distribution of degenerate transition splittings nicely describes the observed spectra in this approximation where the unstrained crystal potential has been ignored. For zero splitting, the required accident that both B and C in Eq. (28) are identically zero has zero probability, and hence there is a notch in the absorption spectrum of Fig. 28. This notch does not go precisely to zero absorption because the tails of the homogeneous line shapes near the notch frequency fill it in.

The asymmetry in the peak heights is described by changes in the transition moments with splitting E_s . As the rotor site is deformed, the lower energy wave functions $\Psi_{k=0,-1}$ become more confined to the two wells of $V_s(\varphi)$, but the higher energy $\Psi_{k=+1}$ wave function is more confined to the peak regions of $V_s(\varphi)$. The lower-energy $K=0$ to -1 transition becomes polarized along the $V_s(\varphi)$ wells and increases approximately linearly in strength, and the

higher energy $K=0$ to $+1$ transition becomes polarized perpendicular to the wells and decreases approximately linearly in strength. Confinement of the wave functions into particular orientations is consistent with the earlier interpretation that the reorientational tunneling modes are converted into localized librational modes at high stress.^{22,23}

G. Estimate of the strain-coupling parameter for the ν_2 fine structure

An estimate for the strain coupling parameter λ_1 can be obtained from the uniaxial stress data shown in Fig. 25. Computing the strain tensor for $[110]$ applied stress in the cubic crystal coordinate system gives

$$\epsilon = -\frac{|\sigma_0|}{2} \begin{pmatrix} S_{11} + S_{12} & \frac{1}{2}S_{44} & 0 \\ \frac{1}{2}S_{44} & S_{11} + S_{12} & 0 \\ 0 & 0 & 2S_{12} \end{pmatrix}, \quad (37)$$

where σ_0 is the applied stress and S_{ij} are the KCl cubic crystal compliances.⁷⁴ Rotating the coordinate system to either of the two distinct groups of $\langle 111 \rangle$ oriented centers with respect to the $[110]$ stress gives

$$C = 0, \\ B = \begin{pmatrix} -\frac{|\sigma_0|}{2} [S_{11} - S_{12} - S_{44}] & \text{for } [111] \text{ and } [11-1] \text{ O-O axes} \\ -\frac{|\sigma_0|}{2} [S_{11} - S_{12} + S_{44}] & \text{for } [-111] \text{ and } [1-11] \text{ O-O axes} \end{pmatrix}. \quad (38)$$

From $E_s = \lambda_1 |B|$, and a fit to the uniaxial stress data in Fig. 25 for stress $< 2 \text{ kg/mm}^2$, an estimate for $\lambda_1 = (1100 \pm 200) \text{ cm}^{-1}$ is obtained.

With the estimate for λ_1 , the width in the distribution of crystal strains w can be compared with the largest plastic deformation $-\Delta l/l = 1\%$ in Fig. 28. A 1% permanent plastic deformation corresponds to a full width in the microscopic crystal strain distribution due to dislocations of $2.35w = 2.35(1.2 \text{ cm}^{-1})/\lambda_1 = 0.26\%$. In other words, the standard deviation of crystal strains at NO_2^- defect sites is comparable to, but less than the total plastic deformation. This is consistent with permanent plastic deformation occurring largely by simple slip accompanied by a smaller amount of induced disorder due to dislocations.⁷⁵

V. SUMMARY AND CONCLUSIONS

New spectral features of the previously unresolved vibrational mode spectra for NO_2^- molecular defects in KI, KBr, and KCl crystals have been found at low temperatures using high-resolution IR interferometry and persistent infrared spectral hole burning separately as well as in conjunction with each other. The absorption features occur in four separate spectral regions, the bending-mode (ν_2) region (around 800 cm^{-1} , see Fig. 5), the asymmetric and symmetric stretch-mode region (1200 to 1350 cm^{-1} , see Figs. 6 and 7), and two vibrational combination mode regions (2000 to

2100 cm^{-1} , see Fig. 8, and 2500 to 2650 cm^{-1} , see Fig. 9). Our main findings are summarized here.

High-resolution FTS spectroscopy indicates a 300-fold range of vibrational mode widths from the 0.01 cm^{-1} wide inhomogeneously broadened $\text{KI}:\text{NO}_2^- \nu_2$ mode to the $\sim 3 \text{ cm}^{-1}$ wide homogeneously broadened ν_1 modes in all three hosts at low temperatures. Unusual V-shaped notches have been resolved for the first time in the inhomogeneously broadened fine structure around the ν_2 bending mode for $\text{KCl}:\text{NO}_2^-$ and $\text{KBr}:\text{NO}_2^-$ defects.

The experimental technique of persistent infrared vibrational-mode hole burning with lead salt diode lasers in low-temperature samples has been demonstrated and characterized in some detail. Our studies show that with a maximum laser intensity of 25 mW/cm^2 , persistent effects can be produced in many of the internal modes and combination bands of NO_2^- molecular defects in alkali halide crystals at 1.5 K.

The union of the IR diode laser and the FT interferometric method has produced a new pump-probe technique which combines the high brightness of the diode laser pump with the broadband capability of FT spectroscopic probe to investigate holes generated far from the laser frequency. In particular, hole burning with simultaneous FTS probing in the V-notched absorption fine structure at the ν_2 mode in $\text{KCl}:\text{NO}_2^-$ has provided the first observation of multiple persistent infrared satellite holes.

Detectable persistent holes are not produced with infrared diode lasers in all of the vibrational modes, and an explanation is found in terms of a competition between hole production and relaxation rates. This competition can be characterized by a specific hole burning intensity parameter $I_h^p = h\nu/\eta\sigma\tau$ [see Eq. (10)]: Below this value the hole relaxation rate overwhelms the hole production rate and holes are suppressed. Alternatively, if the product $\eta\sigma\tau$ is large for an arbitrary system because of a strong hole production pathway η , a large peak cross section σ (produced, say, by narrow mode widths or small effective oscillator mass), or by a slow ground-state relaxation τ , then only small laser intensities are needed to burn a detectable hole for a given level of detection sensitivity.

It is found that the inhomogeneous broadening in the $\text{KCl}:\text{NO}_2^- \nu_2$ tunneling fine structure is dominated by degenerate rotor level splitting produced by weak random strains in the crystalline lattice. An important clue for this identification was the observation of multiple persistent satellite holes. Additional spectroscopic measurements on this ν_2 band with temperature, plastic deformation, and uniaxial stress generated a quantitative picture for the tunneling level diagram and its behavior with crystal strains.

A theoretical model demonstrates that the V-shaped notches in the inhomogeneous broadened ν_2 reorientational tunneling-vibrational absorption bands for NO_2^- in KCl and KBr appear because of degenerate level splitting by two random strain components in the crystal [Eq. (29)]. Strain perturbation of a degenerate level results in an energy splitting that is the square root of a quadrature sum of strain components, rather than a linear sum. The terms in the quadrature sum do not change sign, hence, the number of strain combinations resulting in a specific splitting is restricted. In particular, in smooth distributions of strain components centered about zero strain, there are no centers with zero splitting, and the spectrum of splittings rises linearly from zero, hence the characteristic V-shaped notch. The asymmetry in the peak heights of the ν_2 doublet straddling the V-shaped notch arises from variations in the absorption cross section for the $K' - K = \pm 1$ one-dimensional rotor transitions with lattice strain.

We conclude that this unusual V-shaped inhomogeneous broadening with zero strength at zero splitting is a general feature of inhomogeneous line shapes whenever random strain splitting of a degenerate level dominates the inhomogeneous broadening. Nondegenerate levels perturbed by random crystal strains depend on a linear combination of strain components⁷⁰ so that a Gaussian distribution of strains produces a Gaussian absorption profile with its peak at zero net energy shift. In contrast, random strain splittings of the degenerate levels of the 1D rotor system result in the non-Gaussian shape shown in Fig. 28, which has a minimum rather than a peak at zero splitting.

Persistent IR spectral holes have now been observed for three different symmetry molecules in alkali halide crystals at low temperatures: a spherical top^{56,63,67-69} (ReO_4^-), a diatomic with a near-neighbor impurity⁵⁶⁻⁵⁸ (i.e., $\text{CN}^-:\text{Na}^+$), and a bent triatomic⁴⁴⁻⁴⁶ (NO_2^-), the subject of this paper. It is observed that each system has its own unique hole

burning traits. This high-resolution technique is powerful when it works but not all molecules show this persistent effect; for example, no PIRSH's are found for NCO^- , CN^- , or CN^- pairs.^{56,58}

The likelihood of producing PIRSH's can be parametrized in terms of the product of three quantities: η the hole burning efficiency, σ the cross section, and τ the relaxation time back to the ground state. One method for maximizing the product $\eta\sigma\tau$ in molecular PIRSH burning studies may be to focus on the different barriers to reorientation in different hosts. Some information on the influence of the reorientational barrier height on PIRSH burning is available from $\text{CN}^-:\text{Na}^+$ and NCO^- hole burning studies in KBr,^{57,58} two systems which display a single sharp spectral line near 2100 cm^{-1} at low temperatures. To account for the absence of PIRSH's in the NCO^- lattice system, a large barrier, hence, a very small η , must be invoked. For $\text{CN}^-:\text{Na}^+$ complexes, which do show PIRSH's, the barrier to reorientation is also large (1040 cm^{-1}), which presumably also gives the low $\eta \sim 10^{-6}$ observed for this defect. However, for $\text{CN}^-:\text{Na}^+$, this large barrier produces a very long PIRSH lifetime at 1.7 K. Absence of hole decay by other processes, such as tunneling, makes this combination PIRSH burnable at very small intensities. Why the same reasoning does not apply to the NCO^- lattice system is not yet clear. Perhaps the modes of this molecule-lattice system are lifetime broadened, for some reason, so that spectral holes are not possible.

One way to extend the present work would be to examine the PIRSH burning of molecular defects in the sodium halides. Thermally stimulated depolarization data for NO_2^- doped sodium halides,⁷⁶ suggests that the barriers to molecule reorientation are several times larger than for the potassium salts. If hole decay is also smaller, then PIRSH's should be readily produced with a smaller single mode diode laser intensity than was required in the potassium halides. A reduced intensity requirement for the single mode pump is crucial if a complete high resolution PIRSH study is to be attempted for the different internal modes, sidebands and combination bands using combined diode laser pump and high-resolution IR interferometer probe beams.

ACKNOWLEDGMENTS

The authors wish to acknowledge fruitful discussions with and critical reading of the manuscript by S. P. Love, C. Mungan, D. M. Riffe, and R. H. Silsbee. This work is supported by the Army Research Office, Grant Nos. DAAL03-89-K-0053 and DAAL03-90-G-0040 and by the National Science Foundation, Grant No. DMR-89-18894.

¹ V. Narayanamurti and R. O. Pohl, *Rev. Mod. Phys.* **42**, 201 (1970).

² W. F. Sherman and G. R. Wilkinson, in *Vibrational Spectroscopy of Trapped Species*, edited by H. E. Hallam (Wiley, London, 1973), pp. 246.

³ A. S. Barker and A. J. Sievers, *Rev. Mod. Phys.* **47** Suppl. No. 2, (1975).

⁴ F. Bridges, *Crit. Rev. Solid State* **5**, 1 (1975).

⁵ T. Timusk and W. Staude, *Phys. Rev. Lett.* **13**, 373 (1964).

⁶ K. K. Rebane, R. A. Avarmaa, and L. A. Rebane, *Izv. Akad. Nauk SSSR. Ser. Fiz.* **32**, 1381 (1968).

- ⁷ R. Avarmaa and L. Rebane, *Phys. Status Solidi B* **35**, 107 (1969).
- ⁸ R. Avarmaa and P. Saari, *Phys. Status Solidi B* **36**, K177 (1969).
- ⁹ P. Saari and K. Rebane, *Solid State Commun.* **7**, 887 (1969).
- ¹⁰ A. R. Evans and D. B. Fitchen, *Phys. Rev. B* **2**, 1074 (1970).
- ¹¹ R. V. Avarmaa, *Opt. Spektrosk.* **29**, 381 (1970).
- ¹² P. Saari, *Phys. Status Solidi B* **47**, K79 (1971).
- ¹³ K. K. Rebane and L. A. Rebane, *Pure Appl. Chem.* **37**, 161 (1974).
- ¹⁴ A. M. Freiberg, A. B. Treshchalov, and O. I. Sild, *Zh. Prikl. Spektrosk.* (Engl. trans.) **28**, 548 (1978).
- ¹⁵ A. Freiberg and L. A. Rebane, *Phys. Status Solidi B* **81**, 359 (1977).
- ¹⁶ A. Treshchalov, *Eesti NSV Tead. Akad.* **28**, 233 (1978).
- ¹⁷ A. Treshchalov and L. A. Rebane, *J. Mol. Struct.* **61**, 1 (1980).
- ¹⁸ H. J. Jodl and F. Bolduan, *Phys. Status Solidi B* **103**, 297 (1981).
- ¹⁹ L. A. Rebane and O. I. Sild, in *Proceedings of the International Conference on Defects in Insulating Crystals*, edited by V. M. Tushkevich and K. K. Shvarts (Springer-Verlag, Berlin, 1981), p. 619.
- ²⁰ G. S. Zavt, I. R. Sil'dos, and I. I. Dolindo, *Sov. Phys. Solid State* **26**, 864 (1984).
- ²¹ N. Matsukawa, N. Nagasawa, and G. Kuwabara, *J. Phys. Soc. Jpn.* **54**, 3168 (1985).
- ²² I. Dolindo, O. Sild, and I. Sildos, *Eesti NSV Tead. Akad. Toim. Fuus. Mat.* (in Russian) **36**, 364 (1987).
- ²³ I. Sildos, I. Dolindo, and G. Zavt, in *Proceedings of the International Conference "Phonons 89"*, edited by S. Hunklinger, W. Ludwig, and G. Weiss (World Scientific, Singapore, 1990).
- ²⁴ I. R. Sildos, L. A. Rebane, and V. E. Peet, *J. Mol. Struct.* **61**, 67 (1980).
- ²⁵ F. J. Lohmeier, *Opt. Commun.* **63**, 103 (1987).
- ²⁶ V. Narayanamurti, W. D. Seward, and R. O. Pohl, *Phys. Rev.* **148**, 481 (1966).
- ²⁷ R. Bonn, R. Metselaar, and J. v. d. Elksen, *J. Chem. Phys.* **46**, 1988 (1967).
- ²⁸ R. Kato and J. Rolfe, *J. Chem. Phys.* **47**, 1901 (1967).
- ²⁹ D. E. Milligan and M. E. Jacox, *J. Chem. Phys.* **55**, 3404 (1971).
- ³⁰ Y. P. Tsyshichenko, V. P. Demyanenko, and I. P. Pinkevich, *Phys. Status Solidi B* **55**, 739 (1973).
- ³¹ S. S. Khatri and A. L. Verma, *J. Phys. C* **16**, 2157 (1983).
- ³² S. S. Khatri and A. L. Verma, *Phys. Lett.* **95A**, 191 (1983).
- ³³ S. S. Khatri and A. L. Verma, *J. Phys. C* **18**, 5935 (1985).
- ³⁴ R. Callender and P. S. Pershan, *Phys. Rev. Lett.* **23**, 947 (1969).
- ³⁵ R. Callender and P. S. Pershan, *Phys. Rev. A* **2**, 672 (1970).
- ³⁶ L. A. Rebane, T. Y. Khal'dre, A. E. Novik, and A. A. Gorokhovskii, *Sov. Phys. Solid State* **15**, 2129 (1974).
- ³⁷ J. Haldre, L. A. Rebane, A. V. Liapzev, and A. A. Kiselev, *Phys. Status Solidi B* **70**, 359 (1975).
- ³⁸ H. J. Jodl and W. B. Holzapfel, *Chem. Phys. Lett.* **55**, 259 (1978).
- ³⁹ H. Fleurent, W. Joosen, and D. Schoemaker, *Phys. Rev. B* **41**, 7774 (1990).
- ⁴⁰ A. J. Sievers and C. D. Lytle, *Phys. Lett.* **14**, 271 (1965).
- ⁴¹ K. F. Renk, *Phys. Lett.* **14**, 281 (1965).
- ⁴² H. Bilz, K. F. Renk, and K. H. Timmesfeld, *Solid State Commun.* **3**, 223 (1965).
- ⁴³ A. J. Sievers, in *Localized Excitations in Solids* (Plenum, New York, 1968), pp. 27.
- ⁴⁴ W. P. Ambrose and A. J. Sievers, *Chem. Phys. Lett.* **147**, 608 (1988).
- ⁴⁵ W. P. Ambrose and A. J. Sievers, *Phys. Status Solidi B* **151**, K97 (1988).
- ⁴⁶ W. P. Ambrose and A. J. Sievers, *Phys. Rev. B* **38**, 10 170 (1988).
- ⁴⁷ L. A. Rebane, G. S. Zavt, and K. E. Haller, *Phys. Status Solidi B* **81**, 57 (1977).
- ⁴⁸ P. Sauer, *Z. Phys.* **199**, 280 (1967).
- ⁴⁹ G. K. Pandey, M. Massey, and K. L. Pandey, *Phys. Rev. B* **43**, 4433 (1991).
- ⁵⁰ The notation (N,O,O) will hereafter be employed when a specific isotopic species of NO_2^- is discussed. For example, (14,16,16) refers to the abundant $^{14}\text{N}^{16}\text{O}_2^-$ species, and (14,16,18) is the less abundant $^{14}\text{N}^{16}\text{O}^{18}\text{O}^-$ species.
- ⁵¹ C. H. Henry and R. F. Kazarinov, *IEEE J. Quantum Electron.* **QE-22**, 294 (1986); T. Makino, *Opt. Quant. Electr.* **23**, 575 (1991).
- ⁵² G. Herzberg, *Molecular Spectra and Molecular Structure* (Van Nostrand, Princeton, New Jersey, 1945).
- ⁵³ H. S. Sack and M. C. Moriarty, *Solid State Commun.* **3**, 93 (1965).
- ⁵⁴ The tunneling fine structure has been labeled in a variety of ways depending primarily upon modeling assumptions. Since our results complement those of Avarmaa and Rebane (Ref. 7), we will adopt their *P*, *Q*, and *R* labeling.
- ⁵⁵ As an aside, some of the smaller impurity cluster modes about the main NO_3^- nitrate mode in Fig. 7 exhibit PIRSH burning, which will not be discussed in this paper. Burning some of these NO_3^- modes causes some of the NO_2^- impurity cluster modes about the main $\text{NO}_2^- \nu_3$ mode to change. Hence, some of the impurity cluster modes about the main NO_2^- and NO_3^- modes are $\text{NO}_3^-:\text{NO}_2^-$ impurity clusters in addition to the $\text{NO}_2^-:\text{NO}_2^-$ impurity clusters identified earlier (Ref. 33).
- ⁵⁶ *Persistent Spectral Hole-Burning: Science and Applications*, edited by W. E. Moerner (Springer-Verlag, Berlin, 1988).
- ⁵⁷ R. C. Spitzer, W. P. Ambrose, and A. J. Sievers, *Opt. Lett.* **11**, 428 (1986).
- ⁵⁸ R. C. Spitzer, W. P. Ambrose, and A. J. Sievers, *Phys. Rev. B* **34**, 7307 (1986).
- ⁵⁹ O. Sild, *Eesti NSV Tead. Akad. Toim. Fuus. Mat.* (in Russian) **37**, 52 (1988).
- ⁶⁰ Level degeneracy depends upon the defect symmetry and crystal strains. We make no model assumptions at this point and do not claim to know the $K = 2$ level degeneracy without conclusive experimental evidence.
- ⁶¹ H. F. Arnoldus and T. F. George, *Phys. Rev. Lett.* **66**, 1487 (1988).
- ⁶² U. Fano, *Phys. Rev.* **124**, 1866 (1961).
- ⁶³ W. E. Moerner, A. J. Sievers, and A. R. Chraplyvy, *Phys. Rev. Lett.* **47**, 1082 (1981).
- ⁶⁴ D. M. Kammern, T. R. Gosnell, R. W. Tkach, and A. J. Sievers, *J. Chem. Phys.* **87**, 4371 (1987).
- ⁶⁵ L. Allen and J. H. Eberly, *Optical Resonance and Two Level Atoms* (Wiley, New York, 1975).
- ⁶⁶ S. P. Love and A. J. Sievers, *Chem. Phys. Lett.* **153**, 379 (1988).
- ⁶⁷ W. E. Moerner, A. J. Sievers, R. H. Silsbee, A. R. Chraplyvy, and D. K. Lambert, *Phys. Rev. Lett.* **49**, 398 (1982).
- ⁶⁸ W. E. Moerner, A. R. Chraplyvy, A. J. Sievers, and R. H. Silsbee, *Phys. Rev. B* **28**, 7244 (1983).
- ⁶⁹ T. R. Gosnell, A. J. Sievers, and R. H. Silsbee, *Phys. Rev. Lett.* **52**, 303 (1984).
- ⁷⁰ D. B. Fitchen, in *Physics of Color Centers*, edited by W. B. Fowler (Academic, New York, 1968), p. 331.
- ⁷¹ In molecules other than diatomics, there are three principle moments of inertia *A*, *B*, and *C*, with corresponding rotational constants. NO_2^- in KCl and KBr performs tunneling connected with rotation about the *A* axis.
- ⁷² D. L. Dexter, *Solid State Phys.* **6**, 353 (1958).
- ⁷³ N. W. McLachlan, *Theory and Applications of Mathieu Functions* (Dover, New York, 1964).
- ⁷⁴ J. F. Nye, *Physical Properties of Crystals* (Oxford University, New York, 1957).
- ⁷⁵ One caution is offered in comparing the spectra in various UV studies. A splitting of as much as 2 or 3 cm^{-1} is sometimes observed in both the *R*(0) and *P*(1) bands in UV absorption. In our $\text{KCl}:\text{NO}_2^-$ samples, the *R*(0) and *P*(1) splitting observed for the ν_2 vibrational mode is $\omega_{\lambda_1} = 0.3 \pm 0.08 \text{ cm}^{-1}$. Crystals used in different studies may be heavily strained. From the elastic dipole strain interaction energy λ_1 obtained from uniaxial stress results and the linearly notched inhomogeneous absorption spectrum calculation based on degenerate level perturbation theory, we find that the full width in the distribution of microscopic strains in our freshly cleaved $\text{KCl}:\text{NO}_2^-$ samples is 0.05%.
- ⁷⁶ G. Nierste and F. Fischer, *Phys. Status Solidi B* **108**, 269 (1981).